Since January 2020 Elsevier has created a COVID-19 resource centre with free information in English and Mandarin on the novel coronavirus COVID-19. The COVID-19 resource centre is hosted on Elsevier Connect, the company's public news and information website.

Journal of Molecular Structure 1259 (2022) 132747

Contents lists available at ScienceDirect

Journal of Molecular Structure

journal homepage: www.elsevier.com/locate/molstr

Synthesis, crystal structure, DFT and molecular docking studies of N-acetyl-2,4-[diaryl-3-azabicyclo[3.3.1]nonan-9-yl]-9-spiro-4′-acetyl-2′-(acetylamino)-4′,9-dihydro-[1′,3′,4′]-thiadiazoles: A potential SARS-nCoV-2 Mpro (COVID-19) inhibitor

Ramachandran Rajamanickam[a,*], Rani Mannangatty[b], Jayanthi Sampathkumar[c], Kabilan Senthamaraikannan[b], Barathi Diravidamani[d]

[a] Department of Chemistry, PGP College of Arts and Science (Affiliated to Periyar University-Salem), Namakkal, 637 207, Tamil Nadu, India
[b] Department of Chemistry, Annamalai University, Annamalainagar, 608 002, Tamil Nadu, India
[c] Department of Chemistry, N.K.R Government Arts college for Women (Affiliated to Periyar University-Salem), Namakkal, 637 001, Tamil Nadu, India
[d] Department of Physics, N.K.R Government Arts college for Women (Affiliated to Periyar University-Salem), Namakkal, 637 001, Tamil Nadu, India

ARTICLE INFO

Article history:
Received 7 January 2022
Revised 15 February 2022
Accepted 1 March 2022
Available online 2 March 2022

Keywords:
Azabicyclo[3.3.1]nonan-9-ones
Spiro thiadiazoles
Chalcogen bond
SARS-nCoV-2 M^{pro}
Molecular docking

ABSTRACT

In this paper, we describe the synthesis and crystal structure analysis of N-acetyl-2,4-[diphenyl-3-azabicyclo[3.3.1]nonan-9-yl]-9-spiro-4′-acetyl-2′-(acetylamino)-4′,9-dihydro-[1′,3′,4′]-thiadiazole (**3a**) and N-acetyl- 2,4-[bis(*p*-methoxyphenyl)-3-azabicyclo[3.3.1]nonan-9-yl]-9-spiro-4′-acetyl-2′-(acetylamino)-4′,9-dihydro-[1′,3′,4′]-thiadiazole (**3b**). The title compounds **3a** and **3b** are characterized by 1D NMR and single crystal x-ray diffraction analysis. Non-covalent interactions in a molecule were identified by Hirshfeld surface (d_{norm} contacts and 2D fingerprint plot) analysis. In addition, the existence of chalcogen bond (S•••O bond) in the molecular structures (**3a** and **3b**) are described by NCI-RDG and QTAIM analysis. NBO analysis is employed to describe the orbital interactions and electron transfer between sulfur and oxygen atoms. Molecular docking is carried out for compounds **3a** and **3b** with COVID-19 viral protein SARS-nCoV-2 M^{pro} (PDB ID: 6LU7).

1. Introduction

Spiro heterocyclic structure is a unique feature of a several natural and synthetic products that possess remarkable biological activities [1,2]. The potential use of spiro heterocycles in medicinal chemistry has been well documented owing to their prominent pharmacological properties [3]. The thiadiazole moiety is associated with a broad spectrum of biological activities such as antifungal [4], antioxidant [5], anticonvulsant, antiviral [4], plant growth regulatory [6], CNS depressant [7], and anticancer [8] activitiy. Methazolamide is a thiadiazole based drug being used to treat reduction of high pressure inside the eyes, prevents blindness, nerve damage, and vision loss and glaucoma [9]. Similarly, acetazolamide is an another thiadiazole drug candidate being used as drug for the treatment of epileptic seizure, and periodic paralysis [10].

1,3,4-thiadiazole core has been reported as an electron-deficient nature, electron-accepting ability and good thermal as well as chemical stability [11]. Thus, thiadiazole derivatives are often used to create liquid crystals due to charge-transporting ability, photoconductivity, photoluminescence and mesomorphism [12]. Therefore, development of new spiro-heterocycles having thiadiazole ring is worthwhile from the perspective of medicinal and material chemistry [13,14].

Piperidine is an another heterocyclic compound that found naturally in alkaloids, and its derivatives have good biological and pharmacological properties [15]. On the other hand, the six membered piperidine ring undergoes several conformational changes when introducing electron donating or withdrawing substituents at the nitrogen site. For example, the piperidine ring adopts chair conformation with electron donating substituent (H, CH_3, CH_2Ph) whereas the electron withdrawing group (heteroatom group, COR, NO) on the same site adopts boat conformation [16]. Recently, several piperidine derivatives along with the incorporation of hetero conjugate groups at the nitrogen atom of piperidine ring have been well explored by spectroscopic and X-ray analysis [17–19]. Earlier reports disclosed that the blocking of secondary nitrogen atom in the piperidine ring by electron donating or withdrawing groups, abrupt changes were observed in the ring conformations.

* Corresponding author:
E-mail address: synorgramu@gmail.com (R. Rajamanickam).

https://doi.org/10.1016/j.molstruc.2022.132747
0022-2860/

As a result, the molecule displays different conformation such as chair, boat or twist-boat forms.

The novel coronavirus 2019 (nCoV, also called as COVID-19), is a new strain and highly contagious viral disease. The coronavirus causes a severe acute respiratory syndrome (SARS-nCoV-2), has showed to be the most deadly global health crisis since the 1918 influenza pandemic [20]. The novel virus (SARS-nCoV-2) has proven to be a worldwide unprecedented disaster that affects billions of lives across the world in many ways. Currently, there are no specific treatment options for SARS-CoV-2. Thus, it has been classified that COVID-19 is a very rare disease with a limited number of treatment options [21]. Molecular docking is the preliminary study in the drug designing, which help us to find the possible binding site between lead molecule and protein structure. For Covid-19, several docking studies have been reported to find potential antiviral drugs and vaccines [22–26].

In this paper, we have selected bicyclic ring system that contains both heterocyclic (piperidine) and non-heterocyclic (cyclohexane) rings based on spiro derivatives viz. N-acetyl-2,4-[diaryl-3-azabicyclo[3.3.1]nonan-9-yl]-9-spiro-4′-acetyl-2′-(acetylamino)-4′,9-dihydro-[1′,3′,4′]-thiadiazoles (**3a** and **3b)** to describe the spectral characterization and single crystal structure analysis. Also, the DFT studies have been employed to explore the electronic properties of molecules **3a** and **3b**. In addition, the molecular docking is carried out to extend the scope of molecular structure with novel coronavirus causing protein.

2. Experimental

^{1}H and ^{13}C NMR spectra of **3a** and **3b** were obtained from BRUKER AMX 500 MHz FT-NMR spectrometer using $CDCl_3$ as the NMR solvent, whereas TMS was used as an internal reference. The NMR chemical shift (δ) and coupling constants values were measured in ppm and coupling constants in Hz, respectively.

2.1. Synthesis of compounds *3a* and *3b*

The title compounds **3a** and **3b** were synthesized according to the Scheme 1. Initially, 2,4-diaryl-3-azabicyclo[3.3.1]nonan-9-one thiosemicarbazones (**2a** and **2b**) were synthesized according to the literature precedent [27]. The title compounds **3a** and **3b** were synthesized by modification of our earlier reports [28]. A mixture of 2,4-diaryl-3-azabicyclo[3.3.1]nonan-9-one thiosemicarbazone (**2a** or **2b**, 0.5 g) and 20 mL of distilled acetic anhydride were heated at 60°C on water bath for 6 h. After completion of the reaction, as confirmed by TLC, the reaction mixture was kept in the freezer at overnight and the separated solid was filtered off, dried and purified by column chromatography. The pure crystals of **3a** and **3b** for X-ray diffraction analysis were grown by slow evaporation technique using distilled ethanol.

2.1.1. N-Acetyl-2,4-[diphenyl-3-azabicyclo[3.3.1]nonan-9-yl]-5-spiro-4-acetyl-2-(acetylamino)-Δ^2-1,3,4-thiadiazoline (3a)

^{1}H NMR, (δ=ppm): 6.13 (d, 2H, H-2a & H-4a); 3.30 (d, 2H, H-1e & H-5e); 1.70 (s, 4H, amide CH_3 & H-7a); 1.66 (s, 3H, H-6e, H-8e); 1.30 (d, 2H, H-6a & H-8a); 1.24 (m, 1H, H-7e); 9.67 (bs, 1H, spiro NH); 2.20, 1.90 (s, 3H, amide CH_3); 7.40 & 7.51 (t & bs, 10H, aryl protons): ^{13}C NMR (δ=ppm) $CDCl_3$: 61.58 (C-2 & C-4); 41.38 (C-1 & C-5); 25.61 (C-6 & C-8); 18.30 (C-7); 87.28 (C-9); 27.23, 24.63 & 22.36 (amide CH_3); 176.20, 174.22 & 169.55 (amide C=O); 155.60 (C=N); 142.95, 142.18 (C-2′ & C-4′); 128.53, 126.59, 125.58 (other aryl carbons).

2.1.2. N-Acetyl-2,4-[bis(p-methoxyphenyl)-3-azabicyclo[3.3.1]nonan-9-yl]-5-spiro-4-acetyl-2-(acetylamino)-Δ^2-1,3,4-thiadiazoline (3b)

^{1}H NMR, (δ=ppm): 6.11 (d, 2H, H-2a & H-4a); 3.22 (d, 2H, H-1e & H-5e); 1.75 (bs, 4H, amide CH_3 & H-7a); 1.68 (m, 2H, H-6e & H-8e); 1.34 (d, 2H, H-6a & H-8a); 1.23 (m, 1H, H-7e); 9.73 (bs, 1H, spiro NH); 2.19, 1.90 (s, 6H, amide CH_3); 6.91 (d, 5H, aryl protons *ortho* to OCH_3 group; 7.41 (bs, 3H, aryl protons *meta* to OCH_3 group); 3.82 (s, 6H, OCH_3 group at phenyl group ^{13}C NMR (δ ppm) $CDCl_3$: 61.09 (C-2 & C-4); 41.43 (C-1 & C-5); 25.60 (C-6 & C-8); 16.78 (C-7); 87.45 (C-9); 27.37, 24.65 & 22.57 (amide CH_3); 176.90, 174.01 & 169.37 (amide C=O); 155.32 (C=N); 158.21,158.14 (C-2′″ & C-4′″); 134.94, 134.24 (C-2′ & C-4′); 126.70, 113.93 (other aryl carbons); 55.30 (OCH_3 group at the phenyl group).

2.2. Single crystal X-ray analysis

Colorless rectangular crystals (0.25, 0.20, 0.20 mm for **3a** and 0.20, 0.20, 0.25 mm for **3b**) were used for the data collections. The single crystal X-ray diffraction data were recorded using a CCD area detector at room temperature (273 K). The data reduction and cell refinement were carried out using SAINT/XPREP (Bruker), and APEX2/SAINT, respectively. The crystal structures (**3a** and **3b)** were solved by direct methods using SHELX-97 [29]. All the non-hydrogen atoms were treated anisotropically by the full-matrix least squares method, whereas hydrogen atom bound to the carbon atoms were constrained isotropically. However, the hydrogen atoms bound to the nitrogen atoms refined freely. Graphical molecular illustrations were done with ORTEP 3 for Windows [30]. The Crystallographic information files (CIFs) were deposited in the Cambridge Crystallographic Data Centre. The CCDC number for **3a** and **3b** are 796611 and 793237, respectively. CIF data of **3a** and **3b** can be obtained free of charge from www.ccdc.cam.ac.uk/data_request/cif.

2.3. Hirshfeld surface analysis

The Crystal Explorer 21.5 program was used to generate Hirshfeld surfaces (HS) mapped over d_{norm}, shape-index and curvedness plots [31], as previously studied in reference [32]. The structural input files of **3a** and **3b** were obtained from CIF data. The normalized intermolecular contact distance was denoted as d_{norm} using the following relation.

$$d_{norm} = \frac{d_i - r_i^{vdw}}{r_i^{vdw}} + \frac{d_e - r_e^{vdw}}{r_e^{vdw}}$$

where d_e and d_i define the distance from the Hirshfeld surface to nearest outside and inside the nucleus surfaces, respectively, $r_e{}^{vdw}$ / $r_i{}^{vdw}$ define the van der Waals radii of outside and inside the atoms, respectively. The value of intermolecular contacts (d_{norm}) such as hydrogen bonding, van der Waals radii and steric interaction are distinguished by tricolor code; red-white-blue-colors, respectively. The bright red spots on the Hirshfeld surface show the intermolecular contacts less than their van der Waals radii, whereas the blue region on the HS demonstrates intermolecular contacts longer than their van der Waals radii. However, the white spot on the HS indicates the sum of their van der Waals radii. Further, the π-π interaction between asymmetric units can be detected through the shape index mapped surface as they exhibit adjacent red-blue triangle concave.

2.4. Computational study

All quantum chemical calculations were carried out by using Gaussian 09 software with DFT method at B3LYP/6-311G (d,p) level [33]. Gauss view 5.0.9 was used to prepare and inspect the input

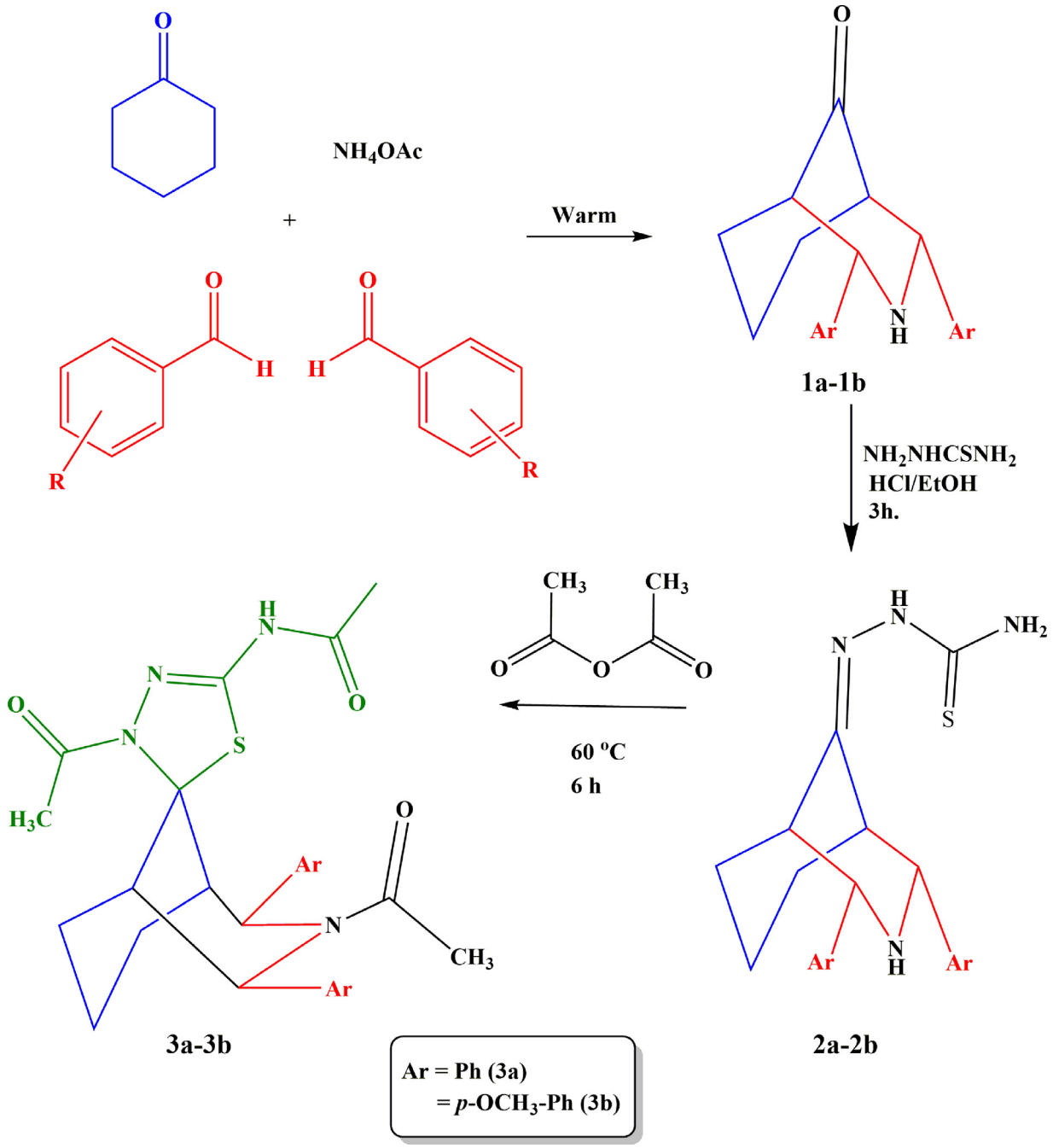

Scheme 1. Synthetic route for the synthesis of compounds **3a** and **3b**

and output files. Quantum theory of atoms in a molecule (QTAIM) was done with AIMALL software [34] whereas non-covalent interaction and radiant density gradient (NCI-RDG) were executed with Multiwin and VMD molecular visualization programmes [35]. The docking study was carried out using AutoDockTools 1.5.7 [36]. The selected protein structure for this study was obtained from Protein Data Bank (PDB ID: 6LU7). Both ligands (**3a** and **3b**) and protein structure (6LU7) were cleaned prior to the docking using Discovery Studio 2021 Client [37]. The grid box was centered using −19.173, 10.969, and 68.039 Å along *x, y, and z* axes was prepared with 70 × 65 × 70 A with spacing of 0.375 Å. The genetic algorithm was employed for ligand **3a** and **3b** as the search parameter with 100 runs.

3. Results and Discussion

3.1. NMR analysis of 3a and 3b

NMR signals were assigned based on the signal position, multiplicity and integral values [38]. The proton and carbon NMR chemical shift values of **3a** and **3b** are presented in section 2.4. It is seen that, two doublets were observed at 6.13 and 3.30 ppm (for **3a**) ppm and 6.11 and 3.22 ppm (for **3b**) with two protons integral each should be assigned to benzylic (H-2/H-4) and bridgehead (H-1/H-5) protons, respectively. The observed chemical shift value of H-2/H-4 is deshielded about 2 ppm as compared to 2,4-diaryl-3-azabicyclo[3.3.1nonane-9-one thiosemicarbazones [27], which

were reported at 4.26/4.36 ppm [27]. The large chemical shift variation should be due to incorporation of acetyl group at the nitrogen site of piperidine ring, where the acetyl group undergoes NCO bond free rotation in NMR time scale. Owing to this, the benzylic protons are deshielded significantly. Further, it was expected that broad signal for benzylic protons, as that of our earlier study on N-chloroactyl-2,6-diarylpiperidin-4-ones [17]. Contrary to this, sharp signal appeared due to perpendicular orientation of acetyl group [39].

Further, a collection of signals for H-2/H-4were observed in the upfield region from 1.24-2.73 ppm are due to signals of methylene protons of cyclohexane ring, as shown in Fig S1-S2. It is seen that, three multiplets appeared at 1.70, 1.66 and 1.30 ppm (for **3a**) and 1.72, 1.60 and 1.28 ppm (for **3b**). It is worth to mention that due to the anisotropy effect of C-C bond, the equatorial proton in methylene carbon of cyclohexane ring is more deshielded than its axial proton. Based on this, the deshielded multiplets at 1.70 ppm (**3a**), and 1.72 ppm (**3b**) is attributed to H-6e/H-8e protons whereas the signal at 1.66 (**3a**), and 1.60 ppm (**3b**) should be due to H-6a/H-8a protons. However, the signal 1.30 ppm (**3a**), 1.28 ppm (**3b**) with one proton integral value is due to H-7e proton. Similarly, a multiplet at 2.61 with one proton value is due to another H-7 proton (H-7a). The chemical shift value of cyclohexane methylene proton of **3a** and **3b** are in good agreement with the earlier report on parent compounds reported by us [27,40]. Additionally, two singlets were resonated at 2.20, 1.90 (**3a**) and 2.19 and 2.20 (**3b**) ppm with six proton integral value should be due to acetyl methyl protons. The signal at the deshielded region 9.67 ppm (**3a**) and 9.73 ppm (**3b**) with one proton integral value is ascribed to N-H proton in the side chain acetylamino group.

^{13}C NMR spectra of compounds **3a** and **3b** are depicted in Fig. S3 and S4 respectively. It is seen that, two signals with equal intensity were observed at 61.58 and 41.38 ppm (for **3a**) and 61.09 and 41.43 ppm (for **3b**) are attributed to benzylic carbons (C2/C4) and bridgehead carbons (C1/C5), respectively. The methylene carbons of cyclohexane ring signals were observed at 25.61 and 18.30 (for **3a**) and 25.60 and 16.78 ppm (for **3b**). Out of which, the deshielded signal at 25.61 and 25.60 ppm in each compound can be assigned to C6/C8 carbons, whereas the shielded signals at 18.30 and 16.78 ppm in **3a** and **3b**, respectively, are due to C7 carbon. Further, the signals at 87.28 ppm (**3a**) and 87.25 ppm (**3b**) respectively for **3a** and **3b** can be assigned to C9 spiro carbon in the molecular structure.

In both compounds (**3a** and **3b**), collection of signals appeared at 176.20, 174.22, 169.55 and 155.60 ppm (for **3a**) and 176.90, 174.01, 169.37 and 155.32 ppm (for **3b**). Among these, signals in the region of 176.20-169.55 ppm (for **3a**) and 176.90-169.33 (for **3b**) are due to amide carbonyl carbons, whereas the signal at 155.60 (for **3a**) and 155.32 (for **3b**) should be due to imine carbon signals. Signals at 27.23, 24.63 and 22.36 ppm (for **3a**) and 27.37, 24.65 and 22.57 ppm (for **3b**) are due to methyl carbon signal in acetyl group. The aryl carbon signals in both compounds were observed in the region of 158-113 ppm. The methoxy carbon signal in **3b** was observed at 55.30 ppm.

3.2. Single crystal X-ray diffraction analysis

The molecular structures with atom-numbering schemes of **3a** and **3b** are shown in Fig. 1a and Fig. 1b, respectively. The structure refinements and selected geometrical parameters are enumerated in Table **1** and Table **2,** respectively. The compounds **3a** and **3b** were crystallized into a monoclinic lattice with P21/c symmetry. Further, all the C–C and C –H bond lengths in the benzene rings were found to be in the normal range and bond angles were found to be approximately 120°. The C-C-C bond angles and C-C-C-C torsion angles of piperidine and cyclohexane rings are greatly deviated from the parent crystal structures [27]. As a result, significant changes are observed in the conformation of saturated cyclic rings.

To describe the conformation of piperidine and cyclohexane rings, the puckering parameters were derived for compound **3b** using X-ray data. Based on the data, one of the six membered (piperidine) ring adopts boat conformation with the puckering parameters being q_2 and q_3 are 0.045 Å and 0.5773 Å, respectively. The total puckering amplitude Q_T and θ were calculated as 0.5791 Å and 4.46° respectively. However, the cyclohexane ring is preferably adopts normal chair conformation with the puckering parameters of q_2 and q_3 were predicted to be 0.136 Å and 0.559 Å, respectively and Q_T and θ were calculated to be 0.575 (2) Å, and 13.73° respectively [41]. Further, the saturated piperidine ring adopts boat conformation as suggested by the torsion angles around the bonds involving the ring atoms N1-C1-C2-C3 and N1-C5-C4-C3 were found as 22.05 and -39.9° (for **3a**) and 41.6 and -24.6° (for **3b**), respectively. These torsion angles suggest that the piperidine ring N1-C1-C2-C3-C4-C5 deviated significantly from the ideal value of 56° reported for the chair conformation of cyclohexane [16]. Therefore, the piperidine preferred to adopt boat conformation. On the other hand, the cyclohexane ring adopts chair conformation as they shows torsion angle of C3-C4-C20-C19 and C3-C2-C18-C19, were found to be -61.71 and 52.4° (for **3a**) and 62.17 and -53.7° (for **3b**), respectively. In both the crystal structures, the phenyl rings C2 and C4 occupy equatorial orientations as they confirmed by bond angles of C12-C1-C2, C12-C1-N1, C6-C5-C4 and C6-C5-N1 are, 112.5, 114.6, 112.1 and 112.2° (for **3a**) and 111.7, 77.9, 113.7 and 112.4° (for **3b**), respectively. The observed bond lengths and bond angles are in good agreement with those observed for similar bicyclic compounds [27,42].

In **3a** and **3b**, the five membered 1,3,4-thiadiazole ring was found to be in flattened boat conformation, as they undergo N-C=O bond free rotation by N-acetyl group. Further, the observed torsion angles of S1-C3-N2-N3/S-C21-N3-N2 are 36.9 /4.03 and -31.62/-4.01 for **3a** and **3b**, respectively, proved that the existence of boat form.

The crystal structures of **3a** and **3b** are packed by several non-bonded contacts such as C-H$^{\delta+}$•••$^{\delta+}$H-C, S•••O, N-H•••O, C-H•••O and C-H•••C$_\pi$ interactions. Out of which, the most important contacts were found as N-H•••O and C-H•••O hydrogen bonds. The hydrogen bonding and other contacts parameters are listed in Table 3. The solid state structure of **3a** are packed in three dimension by N(4)-H(4)•••O(1) and C(16)-H(16)•••O(1), and C(17-C(21)•••C(21), hydrogen bonds with donor-acceptor distances of 2.816 and 3.513, and 3.559 Å respectively. Unlike the crystal structure **3a, 3b** is packed through the water molecule. It can be seen from Table 3, C(27)-H(27) •••O(3), O(6)-H(6)•••O1, N(4)-H(3)•••O(6) are the major hydrogen bonds with donor-acceptor distances of 3.547 and 2.850, and 2.828 Å respectively.

The nature and strength of intramolecular S···O chalcogen bonds play a key role in biological activity and in supramolecular recognition due to presence of sigma hole in the sulfur atom [43,44]. In both crystal structures **3a** and **3b**, the chalcogen interaction geometry is created R_5^2 motifs, which shows the S-O interaction distances of 2.710 Å with ∠C3-S1-O3 angle of 160.46° for 3**a,** whereas for 3**b**, the S-O distance and ∠C3-S1-O3 were found to be 2.798 Å and 156.84° respectively. Further, it was noted that the, the S-O interaction distance was found to be within the vander Waals radii of sum of the S and O atoms [45]. Therefore, we suggest that there is a charge transfer component to this chalcogen interaction. The bond lengths and bond angles of thiadiazole ring is similar to other previously reported crystal structures [46].

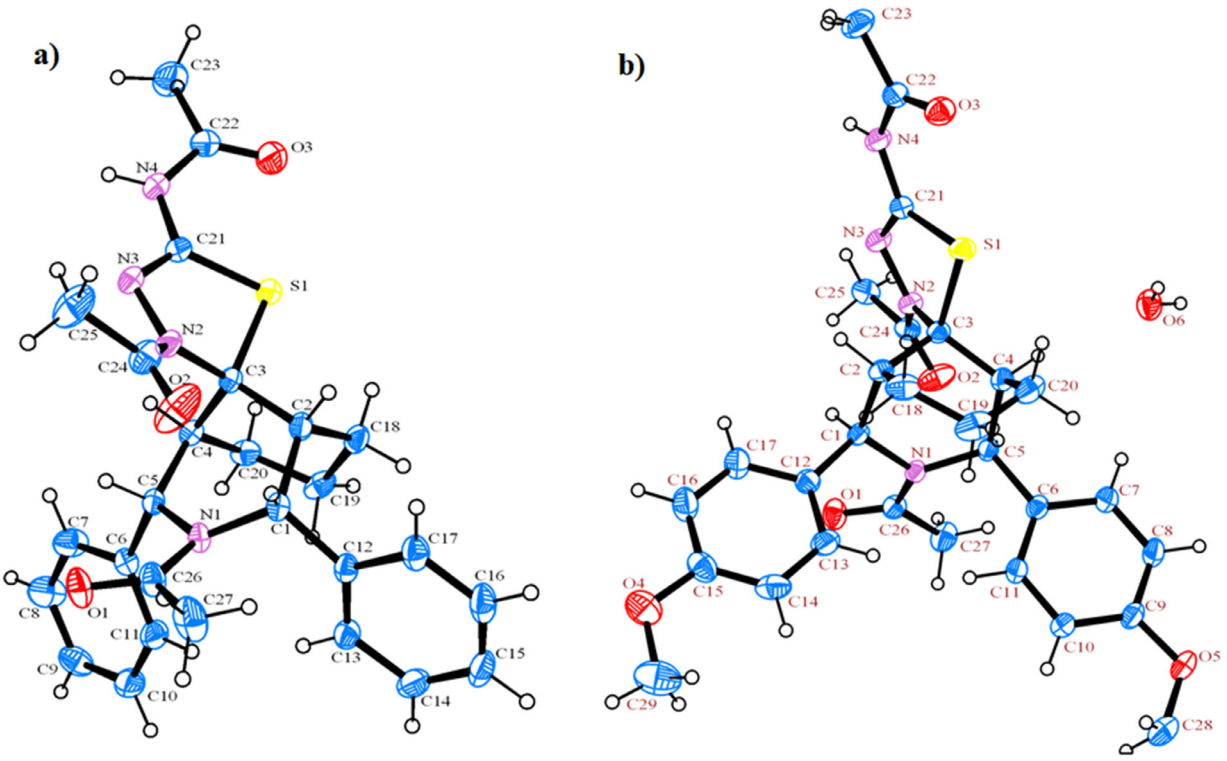

Fig. 1. a) ORTEP diagram of compound **3a**; b) ORTEP diagram of compound **3b.**

Table 1
Single crystal XRD data collection and refinement details of **3a** and **3b**

	Compound **3a**	Compound **3b**
Empirical formula	C_{27} H_{30} N_4 O_3 S	C29 H36 N4 O6 S
Formula weight	490.61	568.68
Temperature	293(2) K	293(2) K
Wavelength	0.71073 A	0.71073 A
Crystal system, space group	Monoclinic, P 21/c	Monoclinic, P 21/c
Unit cell dimensions	a = 9.8486(3) Å; b = 13.8532(3) Å; c = 19.0571(4) Å α = 90 ° deg. β= 101.7150(10) deg. gamma = 90 deg.	a=17.2963(9) b=9.2931(5); c=17.6126(8) α =90.00; β= 97.5020(10) gamma = 90 deg.
Volume	2545.89(11) A^3	2806.8(2)
Z, Calculated density	4, 1.280 Mg/m^3	4, 1.346 Mg/m^3
Absorption coefficient	0.163 mm^{-1}	0.166
F(000)	1040	1208
Crystal size	0.25 × 0.20 × 0.20 mm	0.20 × 0.20 × 0.25 mm
Theta range for data collection	1.83 to 26.18°	1.19 to 26.93°
Limiting indices	-12<=h<=12, -17<=k<=14, -23<=l<=17	-22 =< h =< 21, -11 =< k =< 11, -22 =< l =< 22
Reflections collected / unique	25678 / 5073 [R(int) = 0.0338]	29917 / 6081 [R(int) = 0.037]
Completeness to theta	26.18 99.5 %	26.93° 100 %
Absorption correction	Semi-empirical from equivalents	Semi-empirical from equivalents
Max. and min. transmission	0.9681 and 0.9604	
Refinement method	Full-matrix least-squares on F^2	Full-matrix least-squares on F^2
Data / restraints / parameters	5073 / 0 / 316	6081 / 0 / 369
Goodness-of-fit on F^2	1.040	1.046
Final R indices [I>2sigma(I)]	R1 = 0.0798, wR2 = 0.2466	R1 = 0.0487, wR2 = 0.1402
R indices (all data)	R1 = 0.1008, wR2 = 0.2717	R1 = 0.0707, wR2 = 0.1619
Largest diff. peak and hole	2.841 and -0.333 $e.A^{-3}$	0.686 and -0.456 e.Å-3
CCDC	796611	793237

3.3. Hirshfeld surface analysis

3D Hirshfeld surface and 2D fingerprint plots of compounds **3a** and **3b** were obtained from Crystal Explorer 21.5 to describe the contacts of molecular surface, which have been highlighted with conventional mapping of d_{norm}, as shown in Fig. 2 and Fig. 3, respectively. Due to the presence of multiple electronegative atoms and hydrogen donor group in the title compounds, the crystal structures stabilized through multiple hydrogen bonds. The d_{norm} plots of **3a** and **3b** were mapped with a colour scale range of 0.0432 au (blue) and 1.084 au (red). It can be seen from d_{norm} mapped surface (Fig. 2 and Fig. 3) that there are two major interactions per molecule were detected. As shown in Fig. 2, (for compound **3a**), there are two intense red regions on the oxygen

Table 2
Selected geometrical parameters of **3a** and **3b** obtained from XRD

Compound **3a**					
Atoms	**3a**	**3b**	**Atoms**	**3a**	**3b**
S(1)-C(21)	1.741(4)	1.734(2)	N(3)-C(21)	1.275(5)	1.275(3)
S(1)-C(3)	1.860(3)	1.865(2)	C(5)-C(6)	1.530(5)	1.531(3)
O(1)-C(26)	1.233(4)	1.229(3)	C(1)-C(12)	1.528(4)	1.513(3)
N(1)-C(26)	1.369(4)	1.369(3)	C(1)-C(2)	1.556(5)	1.548(3)
N(1)-C(1)	1.487(4)	1.490(2)	C(4)-C(20)	1.532(4)	1.540(3)
N(1)-C(5)	1.488(4)	1.489(2)	O(2)-C(24)	1.205(5)	1.209(3)
O(3)-C(22)	1.209(5)	1.223(3)	C(2)-C(18)	1.532(5)	1.528(3)
N(2)-C(24)	1.359(5)	1.369(3)	C(19)-C(20)	1.513(5)	1.517(4)
N(2)-N(3)	1.418(4)	1.405(2)	C(26)-C(27)	1.508(6)	1.509(3)
N(2)-C(3)	1.494(4)	1.495(3)	C(22)-C(23)	1.495(6)	1.501(3)
N(4)-C(22)	1.373(5)	1.357(3)	N(4)-C(21)	1.377(5)	1.386(3)
C(21)-S(1)-C(3)	87.60(16)	88.29(9)	N(1)-C(1)-C(2)	113.7(3)	114.70(16)
C(26)-N(1)-C(1)	117.6(3)	112.7(2)	N(3)-C(21)-S(1)	118.0(3)	118.31(16)
C(26)-N(1)-C(5)	113.0(3)	117.2(2)	N(4)-C(21)-S(1)	122.5(3)	123.7(2)
C(1)-N(1)-C(5)	124.2(3)	124.4(2)	N(1)-C(5)-C(6)	112.2(3)	112.40(17)
C(24)-N(2)-N(3)	115.9(3)	114.01(17)	N(1)-C(5)-C(4)	115.6(3)	114.31(16)
C(24)-N(2)-C(3)	132.3(3)	132.60(17)	N(2)-C(3)-C(4)	109.0(3)	120.4(2)
N(3)-N(2)-C(3)	111.6(3)	113.3(2)	N(2)-C(3)-C(2)	121.1(3)	110.5(2)
C(22)-N(4)-C(21)	123.5(3)	125.8(2)	N(2)-C(3)-S(1)	100.2(2)	100.6(1)
C(21)-N(3)-N(2)	109.9(3)	110.35(17)	C(4)-C(3)-S(1)	111.0(2)	108.6(1)
N(1)-C(1)-C(12)	114.7(3)	113.53(16)	C(2)-C(3)-S(1)	108.2(2)	109.5(1)
C3 C2 C1 N1	-22.05	41.6(2)	C3-C2-C18-C19	52.4	-53.7
N1-C5-C4-C3	-39.9	-24.6	S1-C3-N2-N3	36.9	-31.62
C3-C4-C20-C19	61.71	62.17	S-C21-N3-N2	4.03	-4.01

Table 3
Hydrogen bonding parameters of compound **3a** and **3b**

Compound **3a**					
Entry	**Atoms**	**D….A**	**D-H**	**D-H….A**	**D-H….A**
1	S1•••O3^{i}	2.71			
2	N1•••O2^{i}	2.973			
3	N4-H4•••O1^{ii}	2.816	0.86	2.02	153.37
4	C23-H23A•••O1^{ii}	3.506	0.961	2.711	140.5
5	C8-H8•••C14^{iii}	3.634	0.93	2.862	
6	C8-H8•••C15^{iii}	3.534	0.93	2.765	
7	C17-H17•••N4^{iv}	3.453	0.93	2.74	134.17
8	C17-H17•••C21^{iv}	3.559	0.93	2.68	157.91
9	C19-H19A•••C16^{v}	3.612	0.97	2.759	146.98
10	C16-H16•••O1^{vi}	3.513	0.93	2.593	169.97
Symmetry code: (i) x,y,z; (ii) -x,-1/2+y,1.5-z; (iii) 1-x,-1/2+y,1.5-z; (iv) -x,1-y,1-z; (v) 1-x,1-y,1-z; (vi) x,1.5-y,-1/2+z					
Compound **3b**					
Entry	**Atoms**	**D….A**	**D-H**	**D-H….A**	**D-H….A**
1	S1•••O3^{i}	2.798			
2	N1•••O2 ^{i}	2.884			
3	O6-H6•••O1 ^{ii}	2.85	0.827	2.85	166.8
4	N4-H3•••O6 ^{iii}	2.828	0.86	2.828	177.36
5	O6-H6•••O3^{iv}	2.877	0.825	2.877	165.21
6	C28-H28B•••C13^{v}	3.551	0.961	2.764	139.77
7	C25-H25B•••O3 ^{vi}	3.327	0.961	2.449	151.67
8	C29-H29A•••C10 ^{vii}	3.471	0.961	2.874	121.32
9	C27-H27B•••O3 ^{viii}	3.437	0.961	2.559	152.22
Symmetry code: (i) x,y,z; (ii) x,1+y,z; (iii) -x,-y,1-z; (iv) x,-1/2-y,-1/2+z; (v) 1-x,-1/2+y,1.5-z; (vi) -x,-y,1-z; (vii) 1-x,1-y,1-z; (viii) x,1/2-y,-1/2+z					

and nitrogen atoms in the d_{norm} maps, which corresponds to two O…H/H…O contacts belonging to N-H…O (where O from acetyl group and NH from acetylamino group). The donor-acceptor bond distance was found to be 2.344 Å. Further, there are three less intense red spot on the phenyl ring and acetylamino carbon atoms in the d_{norm} maps, corresponds to C…H/H…C contacts belonging to C-G…C. The shape index surface map shows red-blue concave; indicate the presence of π-π stacking interactions in **3a**. Similarly, for compound **3b**, there is a pair of reddish spot on the oxygen atom of d_{norm} map (Fig. 3) corresponds to H…O/O…H contacts belonging to H-O…H (where O from water and H from N-H of acetylamino group, similarly, O-H from water and O from the acetyl group). However, a weak contact was also observed by C-H…O, as shown in weak red spot on the Hirshfeld surface (Fig. 3). In addition, a weak π-π stacking interactions was detected as shown the red-blue triangle concave in shape index (Fig. S5).

2D-fingerprint plot analysis was executed to determine the percentage contribution of intermolecular contacts of **3a** and **3b** with the d_i and d_e distances scales on the graph axes for the total contacts in the range of 0.6-2.6 Å, as shown in Fig. 4 and Fig. 5, respectively. For compound **3a** (Fig. 4), the H••H/H••H and O••H/H••O close contact contribution rate were predicted as 61.6 and 16.5 % at de+di ∼ 1.1 and 0.8-1.2 Å respectively, whereas C••H/H••C and N•••H/H•••N contribution were determined as 15

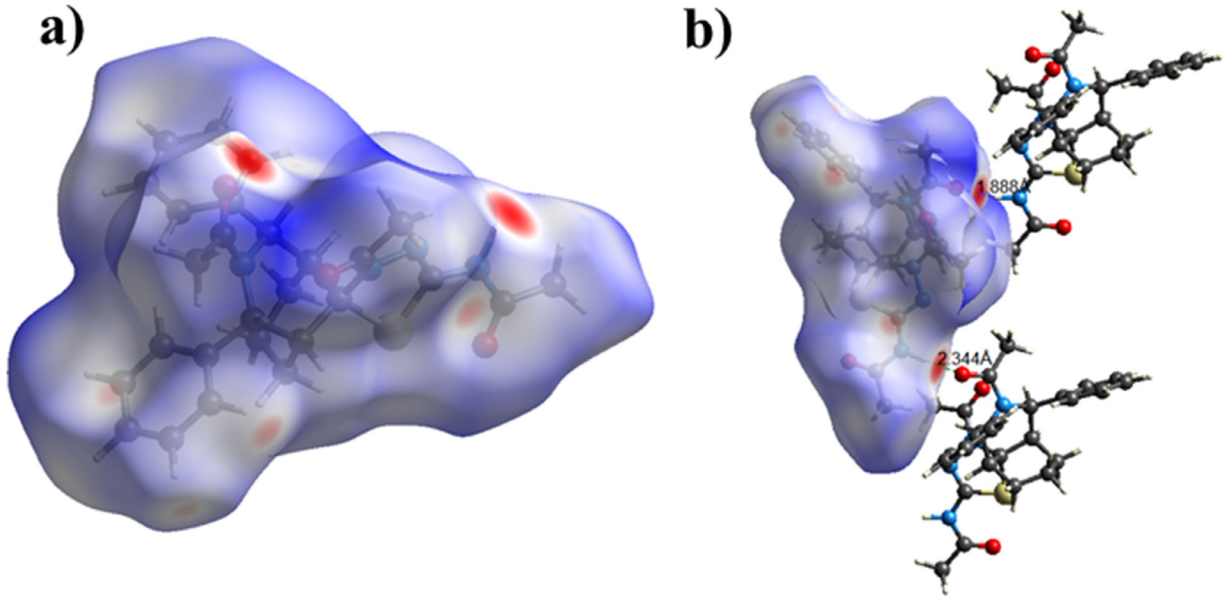

Fig. 2. Hirshfeld surface mapped over (a) d_{norm} (b) d_{norm} mapped on the Hirshfeld surface along with intermolecular interactions of compound **3a.**

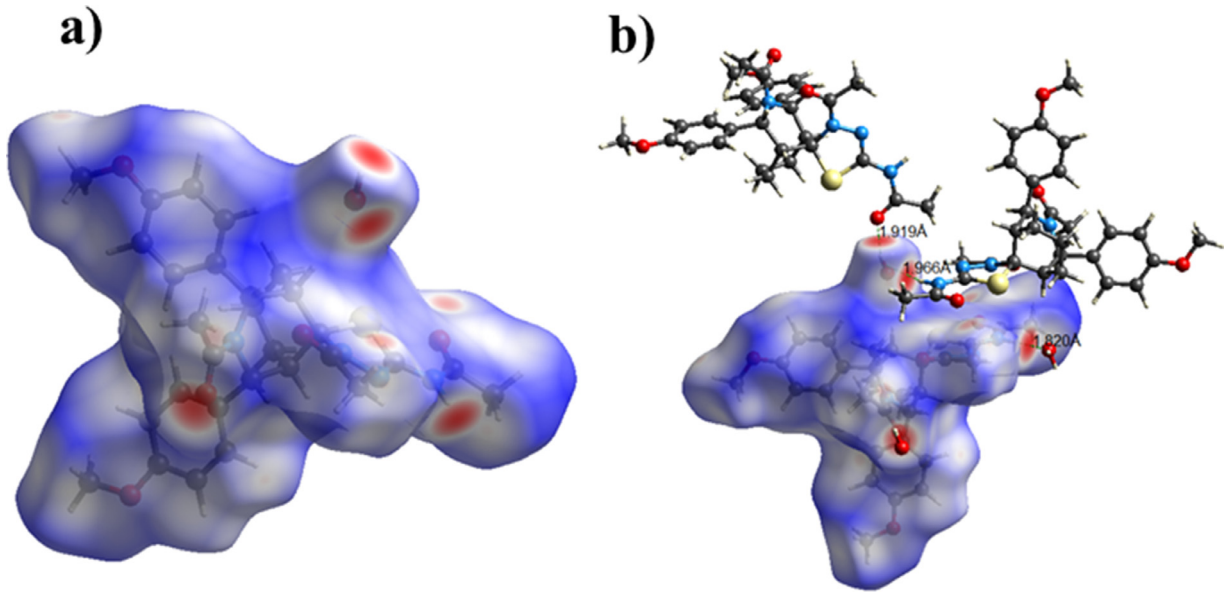

Fig. 3. Hirshfeld surface mapped over (a) d_{norm} (b) d_{norm} mapped on the Hirshfeld surface along with intermolecular interactions of compound **3b.**

and 3.8 % at de+di ~ 1.1 and 1.0-1.6 Å, respectively. Similarly, for compound **3b** (Fig.5), the H••H/H••H and O••H/H••O percentage contributions were found to be 58.6 and 23.7 % at de+di ~ 1.0 and 0.7-1.1 Å respectively. A pair of broad spike peaks were observed for C••H/H••C and N•••H/H•••N contacts at de+di ~ 1.1-1.6 and 1.2-1.7 Å which calculated to be 11.4 and 2.0 % respectively. In both crystals (**3a** and **3b**), the existence of highest percentage contribution of H•••H interaction by 2D-fingerprint plots analysis is in good agreement with the single crystal X-ray analysis.

3.4. QTAIM analysis

Quantum theory of atoms in a molecule (QTAIM) analysis was performed for molecular structures (**3a** and **3b)** to understand the type of non-bonded interactions, particularly classical hydrogen and chalcogen bonds. This can be demonstrated by the bond critical point and electron density topological parameters such as electron density (ρ), positive Laplacian ($\nabla^2\rho$), potential energy density (V) and local kinetic energy density (G), are summarized in Table 4. The bond critical points (BCPs) of molecular structure **3a** and **3b** are shown in Fig. S6. As shown in Fig. S6, bond critical point (ρBCP) was observed between chalcogen atoms (sulfur and oxygen). The electron density ρ and positive Laplacian $\nabla^2\rho$ value were calculated to be 0.017 and 0.053 (for **3a** and **3b** respectively**,** Table 4). The accumulation of electron density ρ in the interaction region and the $\nabla^2\rho$ values at the S•••O chalcogen bond for compound **3a** and **3b** were found to be quite similar to the results from experimental charge density and quantum chemical studies on sulfa-drugs [45]. Further, the crystal structure analysis of compounds **3a** and **3b** show a short S•••O interaction of 2.710 and 2.798 Å with a linear C21-S1-O3 angle of 73.44 and 72.77°, respectively. However, the sum of the Van der Waals radii of sulfur and oxygen atoms are significantly shorter than S•••O interaction. Further, the linearity of the chalcogen bond angle is linked to the nature of n→σ^* interactions.

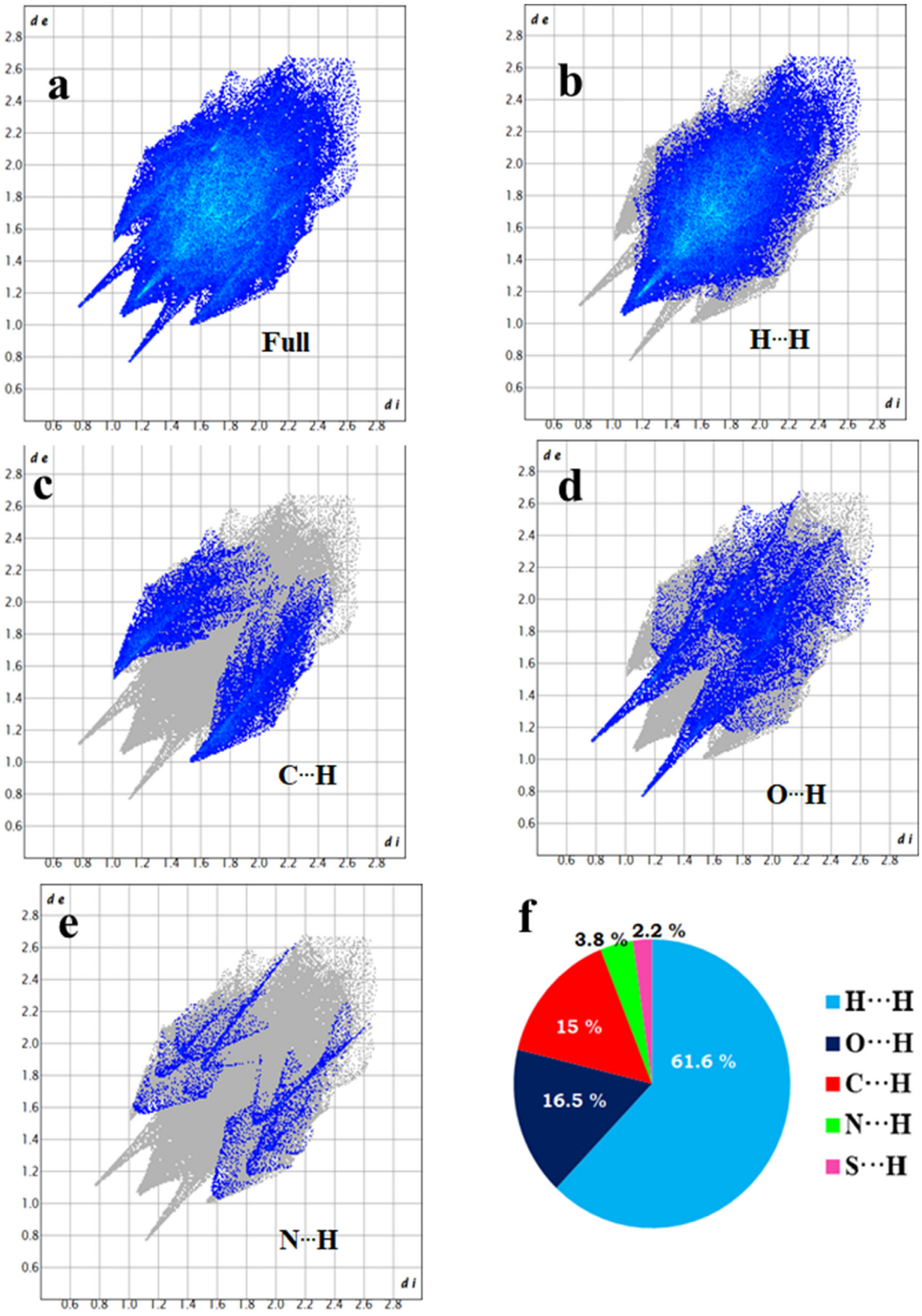

Fig. 4. The 2D fingerprint plots for the **3a** showing the most intercontacts. a) full; b) H…H/H…H (61.6%); (c) C…H/H…C (15.0%); (d) O…H/H…O (16.5%); (e) N…H/H…N (3.8%); (f) percentage contribution of various intermolecular contacts.

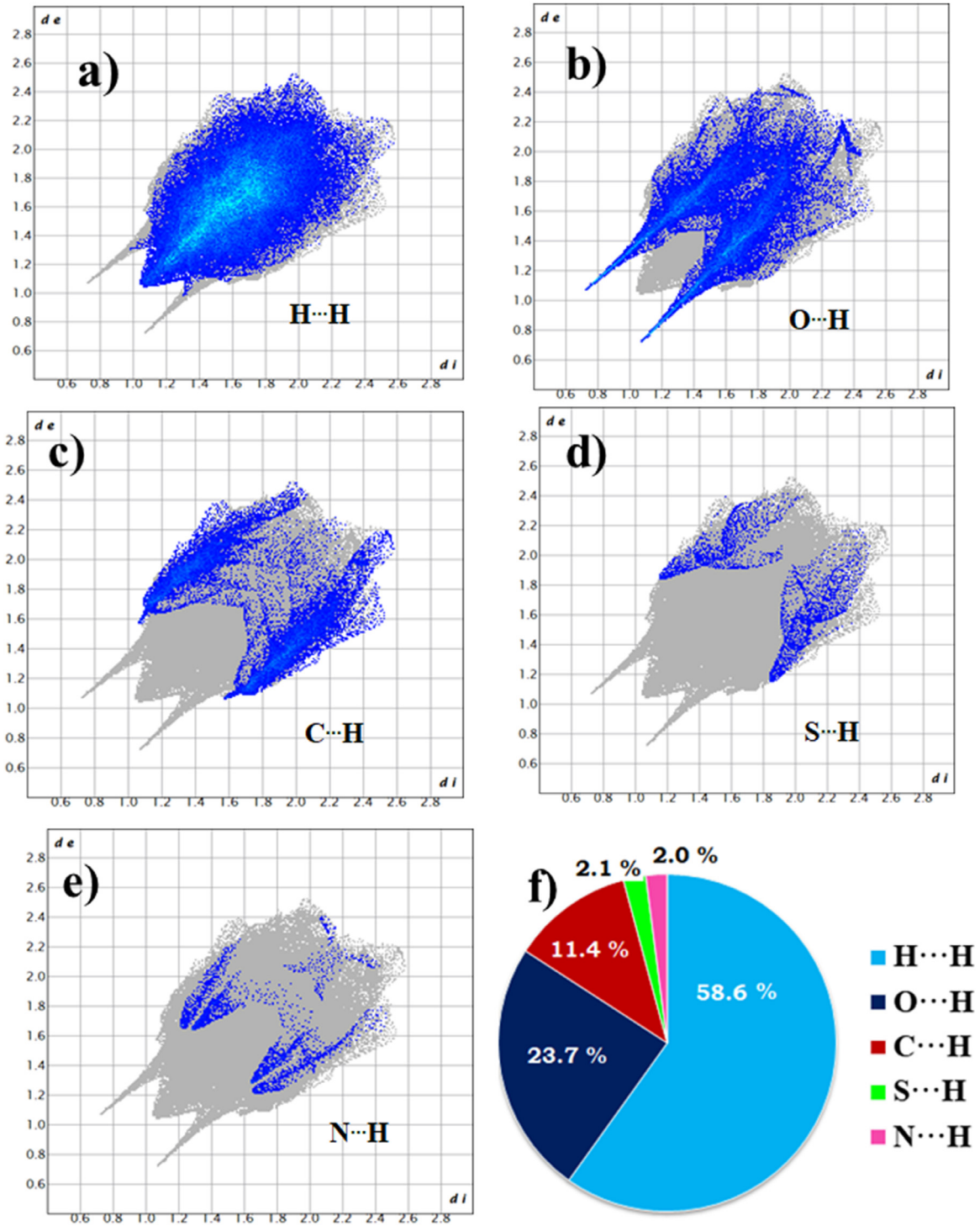

Fig. 5. The 2D fingerprint plots for the **3b** showing the most intercontacts. a) H…H/H…H (58.6%); (b) O…H/H…O (23.7%); (c) C…H/H…C (11.4%); (d) S…H/H…S (1.4%) e) N…H/H…N (2.0%); (f) percentage contribution of various intermolecular contacts.

In addition, other contacts such as C18-H…O17 and C13-H…O17 was observed with 0.0122 and 0.04 (for **3a**) and 0.024 and 0.093 (for **3b**) electron density ρ, and positive Laplacian $\nabla^2\rho$ respectively (Table 4).

3.5. NCI-RDG analysis

Non-covalent interactions-reduced density gradient (NCI-RDG) method was used to explore the various attractive and repulsive forces in a molecule such as H-bond, van der Waals and steric forces. Recently, the classical chalcogen bonding interaction in a molecule has been explored widely using NCI-RDG method [47]. The scatter graph of RDG against $\sin(\lambda^2)\rho$ exploring the type of attractive or repulsive forces that exist in the molecular structure by tri-color scheme (blue-green-red). Blue and green scattering graph at the negative sign indicates attractive forces (hydrogen and chalcogen bonding and van der Waals forces) whereas red spot on the positive sign express the repulsive forces, which mostly

Table 4
QTAIM topological analysis of compounds **3a** and **3b**.

Compound **3a**							
BCP #	**Atoms**	**Rho**	**DelSqRho**	**K**	**V**	**G**	**DelSqV**
1	S1 - O4	0.017166	0.053585	-0.000736	-0.01192	0.01266	-0.04129
2	H14 - O17	0.024281	0.093234	-0.002862	-0.01759	0.020447	-0.13332
3	C20 - H52	0.010473	0.033852	-0.00142	-0.00562	0.007043	-0.02415
4	C24 - H29	0.008146	0.024771	-0.001078	-0.00404	0.005114	-0.0148
5	H29 - H44	0.006226	0.018595	-0.000715	-0.00322	0.003934	-0.00769
6	H25 - H44	0.009692	0.027709	-0.001139	-0.00465	0.005788	-0.01914
Compound **3a**							
3	S1 - O4	0.017056	0.053269	-0.000734	-0.011848	0.012583	-0.040829
18	O6 - H16	0.023652	0.091046	-0.002845	-0.017071	0.019916	-0.125536
26	C9 - H40	0.010041	0.032541	-0.001367	-0.005401	0.006768	-0.022363
51	H23 - H38	0.009399	0.02765	-0.00114	-0.004632	0.005772	-0.016634
63	C9 - H48	0.008472	0.025686	-0.001134	-0.004153	0.005287	-0.014533
64	H38 - H48	0.007647	0.022341	-0.000819	-0.003947	0.004766	-0.009975

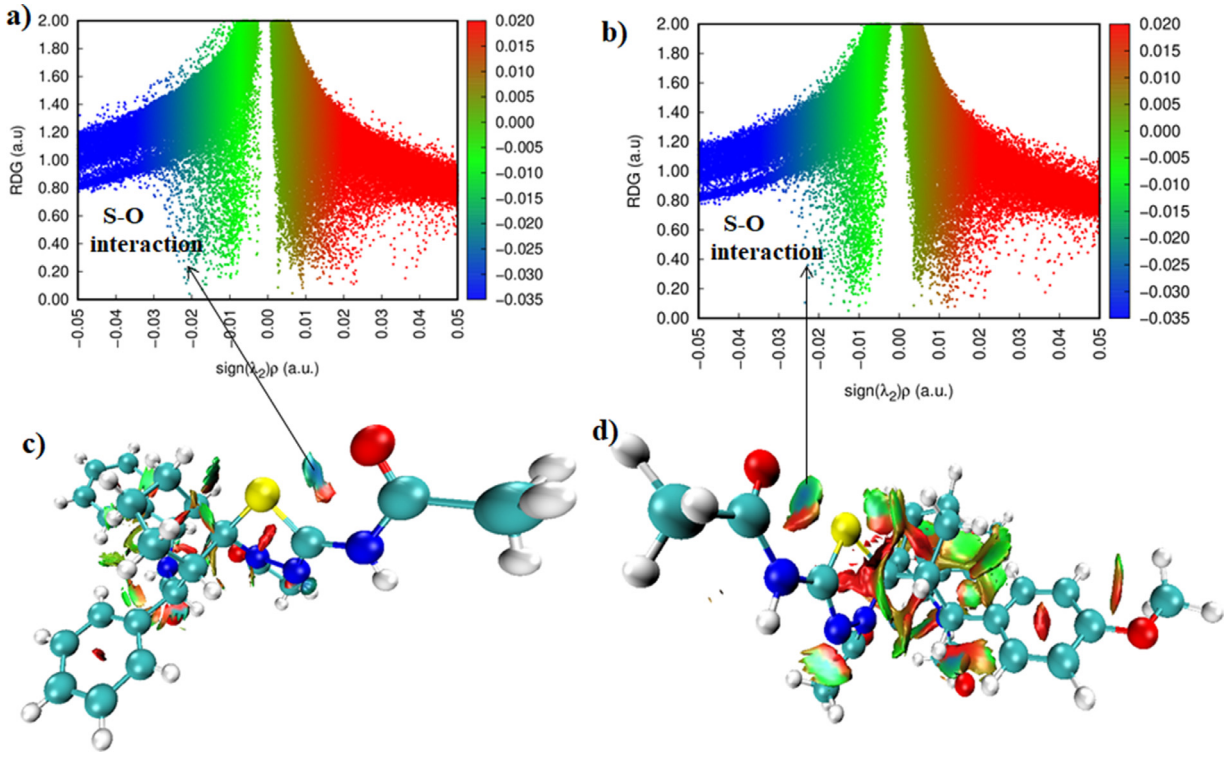

Fig. 6. Non-covalent interactions (NCIs) and reduced density gradient (RDG) Interactions: (a) Compound **3a**; b) Compound **3b**

occurred in the rings. The following relation can be used for the detection of NCI isosurfaces in RDG using this technique.

$$s = \frac{1}{2\left(3\pi^2\right)^{1/3}} + \frac{|\nabla\rho(r)|}{\rho(r)^{4/3}}$$

To get deep understanding the characteristics of intramolecular chalcogen bonds and other forces in a molecules (**3a** and **3b**), the plot of s versus electron density ($\sin(\lambda^2)\rho$) multiplied by the sign of second Eigen value λ_2 was also investigated for compound 3**a** and **3b**, as shown in Fig. 6. It can be seen from Fig. 6a and 6b, the blue scattering spike at the negative sign of $\lambda_2\rho$ (-0.02 a.u) indicate the presence of S•••O intramolecular chalcogen bond. Further, some green peaks were lying at the negative sign of $\lambda_2\rho$ (-0.01 a.u) values illustrate the van der Waals and repulsive forces whereas, the red spots scattering at the positive $\lambda_2\rho$ demonstrates the steric interaction in the molecule **3a** and **3b**. Jindani et al. [48] examined the NCI-RDG analysis for thiazole molecular structure, which showed the electron density (λ_2) value which is similar to the electron density of title compounds **3a** and **3b**.

3.6. DFT study

Density functional theory (DFT) method was employed to inspect the structural geometry (bond lengths and bond angles) and electronic parameters (E_{HOMO} and E_{LUMO}). To describe these, molecular structures **3a** and **3b** were optimized at B3LYP/6-311g(d,p) level, which are depicted in Fig. S7 and S8, respectively. The selected geometrical parameters are presented in Table S1. It can be seen from the Table S1 that the optimized bond lengths and bond angles by theoretical analysis were found to be well replicated with the experimental XRD results, as indicated by the correlation coefficient analysis, Fig. S9 [49]. However, the minor deviations were observed between theoretical and experimental results due to the differences in the molecular environment.

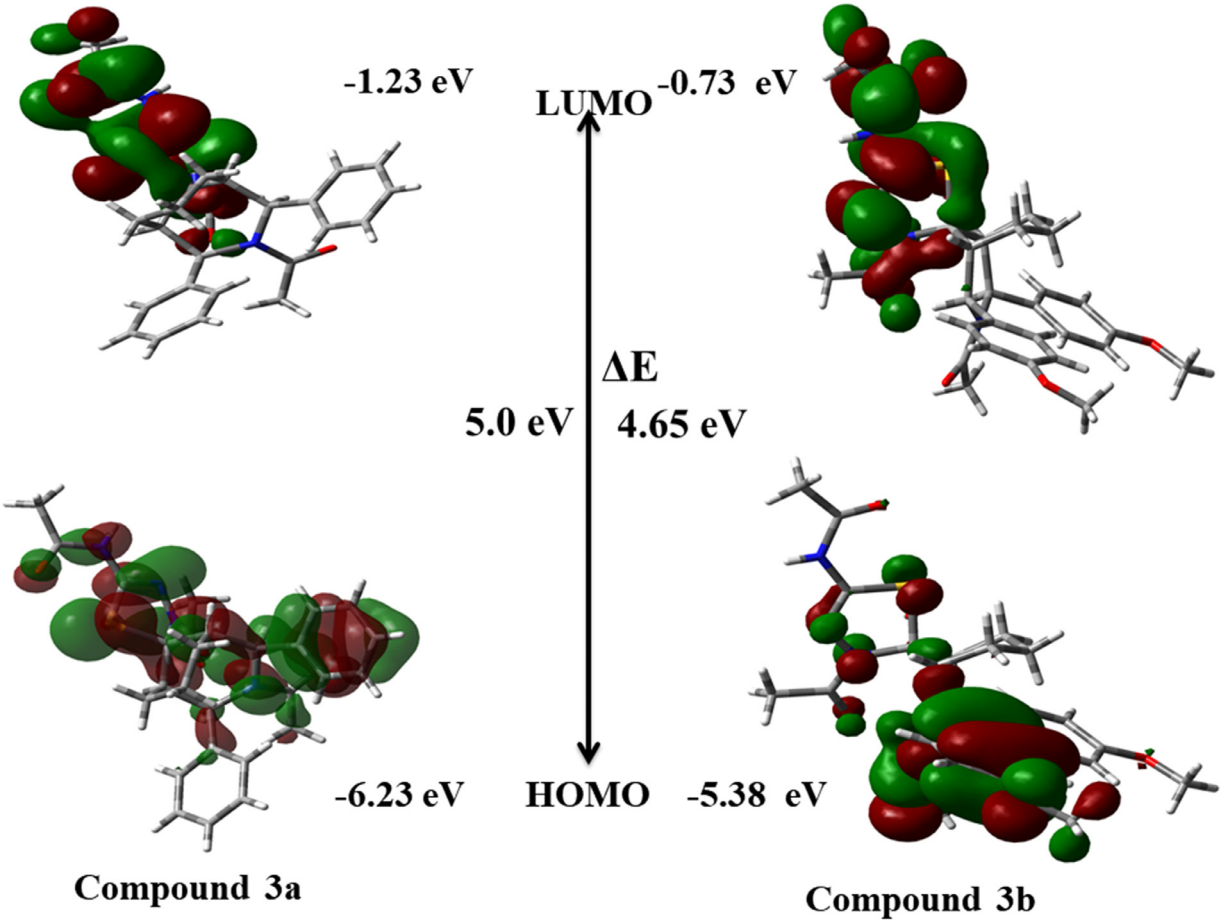

Fig. 7. HOMO/LUMO energy diagram of compounds **3a** and **3b**

In the DFT method of **3a** and **3b**, the C11-S1 bond distance was calculated as 1.90 Å whereas the XRD value found to be 1.86 Å. This should be due to stronger interaction between sulfur and oxygen atoms in the gas phase. However, the non-bonded distance between the sulfur and oxygen in the optimized structures (**3a** and **3b)** were estimated as 2.84 Å (**3a**) and 2.79 Å (**3b**), well less than the combined van der Waals radii of the sulfur-oxygen atoms (3.25 Å) and consistent with the previously reported S–O chalcogen bond distances [50]. The conformational analysis of two six membered rings (cyclohexane and piperidine) were described with torsion angle of the corresponding ring atoms. For **3a**, the observed torsion angle for C3-C4-C20-C19 and C3-C2-C18-C19 were calculated as 52.56 and -61.06° respectively, indicates the cyclohexane ring adopts chair conformation whereas the piperidine undergoes boat conformation with an angle of 26.22 and -41.74° for N1-C1-C2-C3 and N1-C5-C4-C3 respectively. Further, the torsion angle of piperidine and cyclohexane rings are in excellent agreement with the X-ray results. Similarly, for **3b**, the torsion angles of piperidine and cyclohexane rings, C3-C4-C2-C20-C19/C3-C2-C18-C19 and C3-C2-C1-N1/N1-C5-C4-C3, were predicted to be 61.53/-61.90 and 26.20/39.50 respectively.

The frontier molecular orbital (FMO) analysis is widely used to predict the molecular interactions, reactivity, charge transfer, optical and electronic properties of molecules through highest occupied molecular orbital (HOMO) and lowest unoccupied molecular orbital (LUMO). HOMO is the electron rich molecular orbital with high energy (nucleophile) and electron donating capability whereas LUMO is the electron deficient molecular orbital with smaller energy (electrophile) and own electron accepting ability. The energy difference between HOMO-LUMO orbital is called energy gap (ΔE), which is used to describe the stability of molecules. For compounds **3a** and 3**b**, E_{HOMO} and E_{LUMO} values were obtained by the DFT method using B3LYP/6-311 g(d,p) level and the 3D molecular orbital energies of the compounds **3a** and **3b** are depicted in Fig. 7. From the Fig. 7, the band gap energy (ΔE) between HOMO and LUMO orbitals were found to be 5.0 and 4.65 eV, respectively for **3a** and **3b.** It can be further discussed that **3b** shows about 0.5 eV less compared to **3a** due to the presence of electron donating methoxy substituent in the phenyl group, which further increase the electron delocalization.

Further using the energy of HOMO-LUMO orbitals, global chemical reactivity descriptor (GCRD) such as electron affinity (EA), ionization potential (IP), Electronegativity (χ), hardness (η), softness (S) potential (μ), and electrophilicity index (ω) were calculated. The calculated GCRD parameters are presented in Table 5. It is seen that the chemical hardness and softness were calculated to be 0.20 and 0.21 eV for **3a** and **3b**, respectively. Therefore, the molecule **3a** and **3b** have good chemical stability and strength. However, the electronegativity (χ), and chemical potential (μ), were estimated as -3.73 / -3.05 eV; and 3.73 / 3.05 eV, respectively for **3a / 3b.** From the Table 5, it can be concluded that the GCRD parameters of molecule **3b** is significantly lower due presence of methoxy group at the phenyl substituent.

The molecular electrostatic potential (MEP) of an organic molecule can be defined in terms of total charge distribution of the molecule. 3D MEP surface encompassing different color scheme between blue to red, are depicted in Fig. 8a (for **3a**) and Fig. 8b (for **3b**), generated from the optimized structure at B3LYP/6-311 g(d,p)

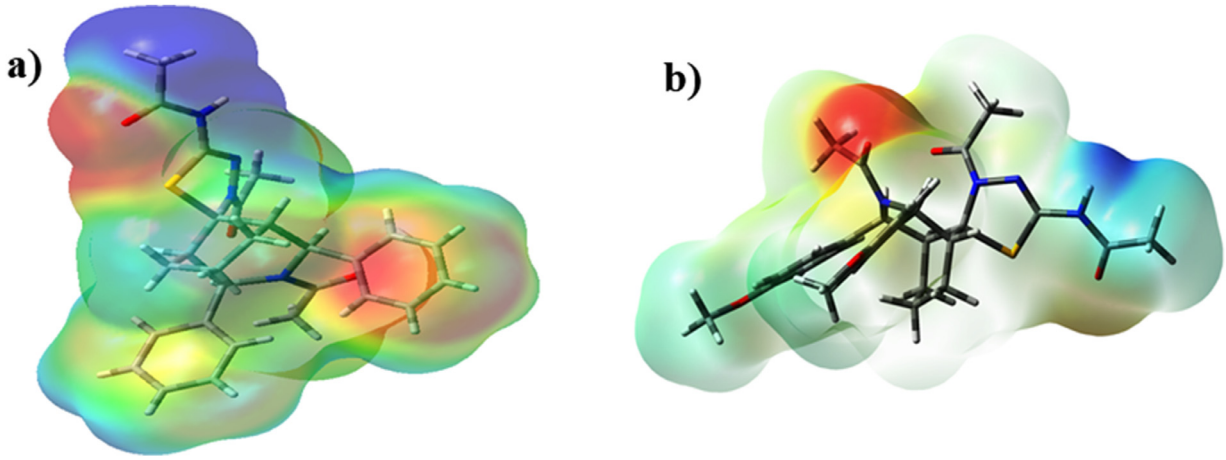

Fig. 8. MEP Map of the compounds **3a** and **3b**.

Table 5
Calculated energy values of **3a** and **3b** at B3LYP/6–311 G (d, p) method.

Quantum Descriptors (eV)	**Compound 3a**	Compound **3b**
E_{HOMO}	-6.23 eV	-5.38 eV
E_{LUMO}	-1.23 eV	-0.73 eV
Ionization potential (IP)	6.23 eV	5.38 eV
Electron affinity (EA)	1.23 eV	0.73 eV
Energy gap (ΔE)	5.0 eV	4.65 eV
Electronegativity (χ)	-3.73 eV	-3.05 eV
Chemical potential (μ)	3.73 eV	3.05 eV
Chemical hardness (η)	2.50 eV	2.32 eV
Softness (σ)	0.20 eV	0.21 eV
Electrophilicity (ω)	2.78 eV	2.00 eV

level. It is seen that red, blue and green are the three major color scheme, which define the electrostatic potential value. Further, the color scheme expands in the order of blue > green > yellow > orange > red. Out of which, the blue regions on the surface signify the positive potential corresponds to the electron deficient site and favor for nucleophilic attack, whereas the red surface region with negative potential, corresponds to electron rich regions and favor for electrophilic reactivity. The green color on the MEP surface indicates zero potential. In addition, the pale blue and yellow colors on the surface map denote the slightly electron deficient and electron rich areas, respectively. For **3a**, (Fig. 8a) the red and yellow region are corresponds to the negative electrostatic potential which associated with electron rich regions (high electron density) such as electronegative groups, and targeted by electrophiles whereas the blue region indicates the positive electrostatic potential (low electron density) which found mostly on the alkyl groups and associated with nucleophilic attack. For compounds **3b**, (Fig. 8b), the negative potential is dominated over the carbonyl group whereas the positive potential exists only on the N-H group.

3.7. NBO analysis

As the presence of sulfur and oxygen atoms close in the molecular structure (**3a** and **3b**), we sought to evaluate the strength of S•••O (chalcogen bonding) interaction. To do this, NBO analysis was performed to get better understanding of inter and intra molecular charge transfer and electron delocalization between filled Lewis type orbital (bonding) and empty non-Lewis type orbital (anti-bonding) of **3a** and **3b** using DFT method at B3LYP/6-311g(d,p) level. The 2nd order perturbation energies of **3a** and **3b** were used to predict the strength and type of interaction between donor and acceptor orbitals, and the interacting stabilization energy. Further, the stabilization energy E(2) is used to define the hyper conjugative interactions and charge transfers in a molecule. Larger stabilization energy provides a stronger interaction between donor and acceptor atoms. Therefore, it is concluded that the stabilization energy E(2) is closely associated with each donor and acceptor NBO orbitals which are denoted as (i) and (j), respectively. The energy delocalization between each donor NBO (i) and acceptor NBO (j) can be predicted using the given equation:

$$E^{(2)} = \Delta E_{ij} = q_i \frac{F_{i,j}^2}{\varepsilon_j - \varepsilon_i}$$

The electron delocalization and its stabilization energies E(2) of **3a** and **3b** are presented in Table S2-S3. Based on the results presented in Table S2 - S3, a number of σ-$\sigma*$, $\pi \rightarrow \pi*$, n$\rightarrow\pi*$, and n$\rightarrow\sigma*$, intramolecular charge transfer processes observed for compounds **3a** and **3b**. Also, the results revealed that the significant

Table 6
The dipole moment (μ) (Debye), polarizability (α) and first hyperpolarizability (β) of **3a** and **3b**

Parameter	**3a**	**3b**	**Parameter**	**3a**	**3b**
α_{xx}	-177.40	-175.31	β_{xxx}	234.1427	-122.88
α_{xy}	16.37	-4.72	β_{xxy}	34.1925	100.94
α_{yy}	-213.46	-243.03	β_{xyy}	-1.6442	32.70
α_{xz}	21.40	-19.97	β_{yyy}	12.4273	42.42
α_{yz}	6.44	-11.87	β_{xxz}	21.6636	-13.68
α_{zz}	224.12	-251.81	β_{xyz}	-1.9129	-4.78
α_{total}	8.18×10^{-24}	33.05×10^{-24}	β_{yyz}	-19.7101	-38.09
μ_x	4.18	-1.6750	β_{xzz}	11.6066	14.11
μ_y	0.32	1.5398	β_{yzz}	-14.7295	1.02
μ_z	1.1273	-2.6231	β_{zzz}	24.7215	0.79
μ_{total}	4.34	3.47233	β_{total}	2.136×10^{-30}	9.145×10^{-29}

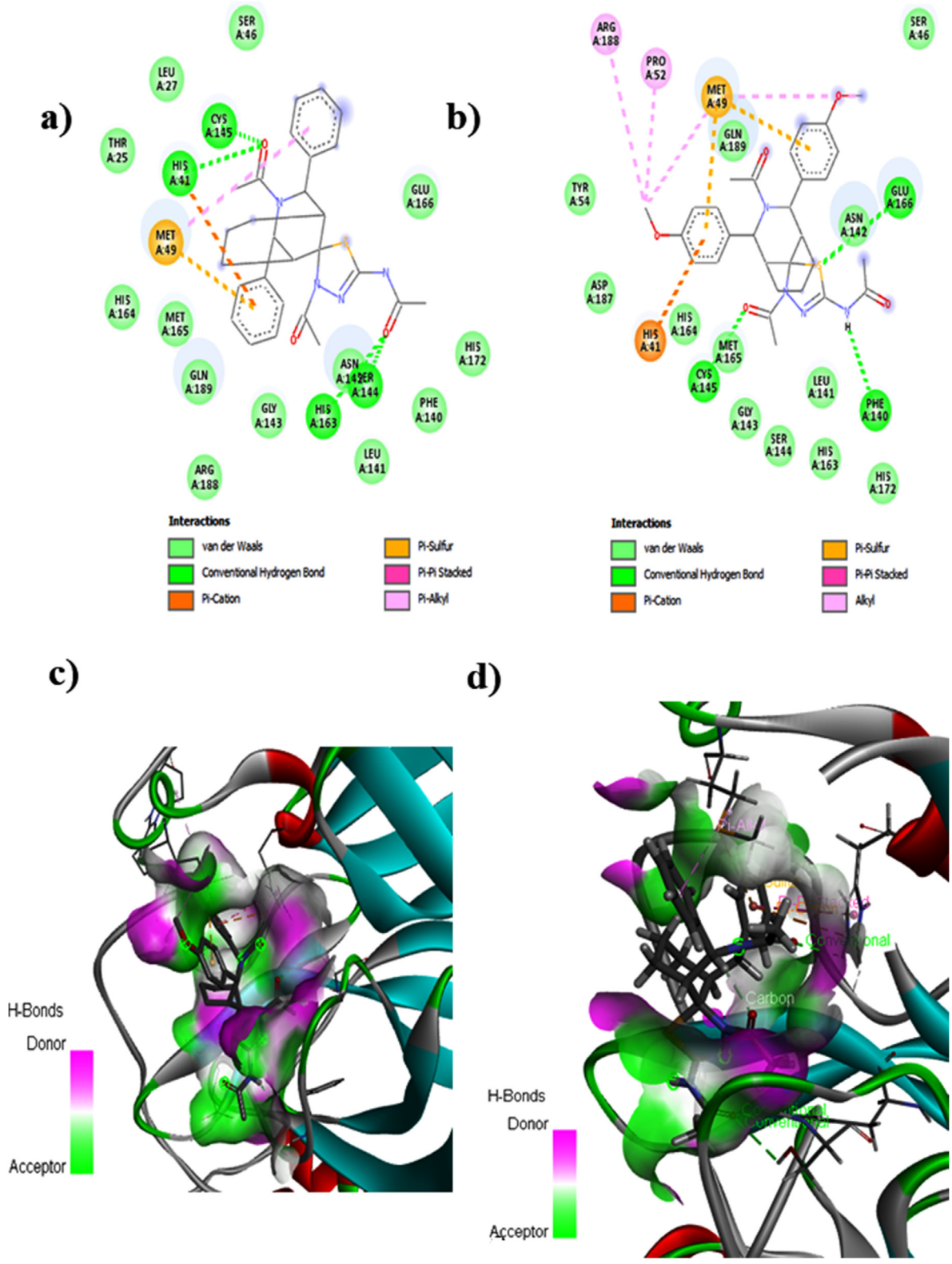

Fig. 9. a) and b) show two dimensional binding interaction between ligands **3a** and **3b** with active site of 6LU7 amino acid residues; c) and d) Compounds **3a** and **3b** show hydrogen bonds interactions with SARS-nCoV-2 Main protease (PDB: 6LU7) active site

orbital interaction between the oxygen lone pair (donor-bonding) and sulfur-carbon antibonding (acceptor) orbital (S−C σ^* orbital), in **3a** and **3b** were calculated as 2.01 kcal/mol (O4 LP → S1-C11 σ^* orbital) and 1.99 kcal/mol (O4 LP → S1-C17 σ^* orbital, respectively.

3.8. NLO Study

Theoretical NLO study was explored for spiro thiadiazole compounds **3a** and **3b** by quantum chemical calculation to estimate the NLO efficiency. The relationship between NLO property and

molecular structure was studied theoretically with the aid of dipole moment, polarizability and hyperpolarizability, which have been calculated using B3LYP/6-311g(d,p) level and the results are summarized in Table 6. Based on the data presented in Table 6, the dipole moment (μ), polarizability and hyperpolarizability values were predicted to be 4.34 Debye, 8.18 $\times$ 10^{-24} e.s.u and 2.136 $\times$ 10^{-30} e.s.u. (for **3a**); 3.47 Debye, 33.05 $\times$ 10^{-24} e.s.u and 9.145 $\times$ 10^{-29} e.s.u. (for **3b**), respectively. The calculated first order hyperpolarizability value is significantly higher than that of urea, which has been used as the reference value for many organic compounds [26]. Therefore, the high values of first order hyperpolarizability reveal that the synthesized spiro compounds **3a** and **3b** have efficient NLO behavior.

It should be mentioned that the NLO of organic material originates from delocalized electron density of the substituents. In this case, both **3a** and **3b** were found to be polar in nature and have non zero dipole moment components. However, out of **3a** and **3b**, compound **3b** contains electron donating *p*-methoxy phenyl group which further increase the electron delocalization. Therefore, **3b** exhibits greater (βo) values than their unsubstituted phenyl group based spiro thiadiazole **3a**.

3.9. Docking study

Molecular docking has proven to be highly efficient method for screening potential drug candidates against specific disease by using computer aided design [51]. Studies of ligand binding to receptor proteins using molecular docking provide insights into the effectiveness of the interactions. Recent studies have identified that the main protease (M^{pro}) of SARS-CoV-2 have consist of three domain such as, domain I (residues 8–101), domain II (residues 102–184) and domain III (residues 201–303), which were similar to other coronaviruses, COVID-19 viral protein (SARS-CoV-2 M^{pro}) also reside a similar catalytic dyad (Cys145-His41), located in a cleft between domain I and II [52,53]. Further, these catalytic dyads of M^{pro} are the major protease activity [54]. It was disclosed that inhibition of M^{pro} catalytic dyad was found to be potential and attractive target for designing and screening of anti-coronavirus drug [55]. Also, it was reported that no specific therapeutic agents or vaccines yet to be identified to treat the infection caused by COVID-19. However, only few clinically trial antiviral drugs such as antimalarial, and anti HIV have been used as the supportive measures to treat COVID-19 infections [55,56]. Virtual screening of molecular docking provides an alternative approach to screen the potential drug candidates for the specific illness at relatively short time.

Studies have been reported various therapeutic options against the COVID-19 causing protein (SARS-CoV-2) through molecular docking studies [57,58]. The docking studies have been applied on compounds **3a** and **3b** with "6LU7" protein which was taken from protein data bank (PDB ID: 6LU7). To examine the protein-ligand binding affinity, 6LU7 and lead compounds (**3a** and **3b**) were fitted to interact with the active site of amino acid residues by using autodock tools. The obtained binding interactions are shown in Fig. 9a and Fig. 9b of **3a** and **3b** respectively. The docking results showed that the lead compounds **3a** and **3b** are formed various binding interactions including H-bond, π-cation, and π-sulfur interactions. Also, this Fig. 9 presents the best docked poses of our ligand in 6LU7. It can be seen from Fig. 9a, Compound **3a** showed significant binding affinity with His41, Met49, Ser144, Cys145, and His163 residues, whereas lead compound **3b** (Fig. 9b) showed interactions with His41, Met49, Pro52, Phe140, Asn142, Cys145, Glu166, and Arg188 residues of $3CL^{pro}$. Among these, His41, Ser144, Cys145, and His163 (for **3a**) and Phe140, Cys145, and Glu166 (for **3b**) displays conventional hydrogen bonding, whereas Met49 forms π-cation, and π-sulfur interactions with compounds **3a** and **3b**. "Further, it can be seen in Fig. 9, the carbonyl group of acetyl function in **3a** exhibits conventional hydrogen bonding with His41, Ser144, Cys145, and His163 residues (Compound **3a**). Unlike **3a**, in compound **3b,** sulphur atom in thiadiazole ring and amino group of acetylamino function show hydrogen bond with Phe140, and Glu166 residues. The interacting amino acid residues were compared with earlier reports [25,26,59], which showed that the residues His41 and Cys145 are the major catalytic active residues in 6LU7. Interestingly, lead compounds **3a** and **3b** exhibit similar binding affinity with His41 and Cys145 amino acid residues. The binding energies of **3a** and **3b** were calculated to be -7.90 and -7.85 kcal/mol, (Table S4) [60]. As clearly seen from Table S4, the existence of methoxy function in the phenyl group was found to be insignificant contribution towards the binding affinity". In conclusion, the above docking results proved that the ligands **3a** and **3b** could be the potential lead molecule for antiviral drug against SARS-nCoV-2 M^{pro}.

4. Conclusion

Thiazole based spiro derivatives **3a** and 3**b** were synthesized and characterized by spectroscopic and single crystal X-ray diffraction techniques. Both the NMR and XRD results proved that the bicyclic rings adopt chair and boat conformation of cyclohexane and piperdine rings, respectively. The asymmetric unit of crystal structures **3a** and **3b** are stabilized mainly due to chalcogen bond, whereas as the crystal packing is stabilized due to divalent hydrogen bond, C-H•••π, C-H•••O, O-H•••C, O-H•••N and H•••H interactions. 3D Hirshfeld surfaces and 2D fingerprint plots analysis were considered to visually spot the different interactions within the molecular structures. Based on the results, the structures **3a** and **3b** were stabilized through H…H, O…H/H…O, C…H/H…C, and N…H/H…N contacts. Further, the 2D fingerprint plot analysis revealed that conventional hydrogen bonding contribution O…H/H…O was calculated to be 16.7 and 23.5 % (respectively for **3a** and **3b**), which could be the strong interaction to stabilize the crystal packing. The presences of chalcogen bond in the studied compounds were identified from the NCI-RDG and QTAIM analyses. NBO analysis suggests that the intramolecular charge transfer between oxygen and sulfur and hyperconjugative interactions are dominated in the molecular structure. NLO study showed that the significant response as compared to the prototype molecule (urea). Finally, the molecular docking study was explored for the compounds **3a** and **3b** with COVID-19 viral protein (SARS-nCoV-2 M^{pro}, 6LU7). The results revealed that the various interactions strongly anchored the lead compounds to the active sites with minimum binding energy, which was calculated to be -7.90 and -7.85 kcal/mol for **3a** and **3b,** respectively.

Declaration of Competing Interest

The authors declare that they have no known competing financial interests or personal relationships that could have appeared to influence the work reported in this paper.

Supplementary materials

Supplementary material associated with this article can be found, in the online version, at doi:10.1016/j.molstruc.2022.132747.

CRediT authorship contribution statement

Ramachandran Rajamanickam: Methodology, Formal analysis, Data curation, Writing – review & editing. **Rani Mannangatty:**

Methodology, Investigation, Formal analysis. **Jayanthi Sampathkumar:** Software, Data curation, Investigation. **Kabilan Senthamaraikannan:** Formal analysis, Investigation. **Barathi Diravidamani:** Software, Data curation, Investigation.

References

[1] I. Natsutani, R. Iwata, Y. Yamai, K. Ishida, Y. Nagaoka, T. Sumiyoshi, Design, synthesis and evaluations of spiro-fused benzoxaborin derivatives as novel boron-containing compounds, Chem. Biol. Drug Des. 93 (2019) 657–665 https://doi.org/, doi:10.1111/cbdd.13496.

[2] M. Moghaddam-Manesh, D. Ghazanfari, E. Sheikhhosseini, M. Akhgar, MgO-Nanoparticle-Catalyzed Synthesis and Evaluation of Antimicrobial and Antioxidant Activity of New Multi-Ring Compounds Containing Spiro[indoline-3,4′-[1,3]dithiine], ChemistrySelect 4 (2019) 9247–9251 https://doi.org/, doi:10.1002/slct.201900935.

[3] S. Balasubramanian, C. Ramalingan, G. Aridoss, S. Kabilan, Synthesis and study of antibacterial and antifungal activities of novel 8-methyl-7,9-diaryl-1,2,4,8-tetraazaspiro[4.5]decan-3-thiones, Eur. J. Med. Chem. 40 (2005) 694–700 https://doi.org/, doi:10.1016/j.ejmech.2005.02.001.

[4] B. Chudzik, K. Bonio, W. Dabrowski, D. Pietrzak, A. Niewiadomy, A. Olender, K. Malodobry, M. Gagoś, Synergistic antifungal interactions of amphotericin B with 4-(5-methyl-1,3,4-thiadiazole-2-yl) benzene-1,3-diol, Sci. Rep. 9 (2019) 12945, doi:10.1038/s41598-019-49425-1.

[5] H. Muğlu, M. Akın, M.S. Çavuş, H. Yakan, N. Şaki, E. Güzel, Exploring of antioxidant and antibacterial properties of novel 1,3,4-thiadiazole derivatives: Facile synthesis, structural elucidation and DFT approach to antioxidant characteristics, Comput. Biol. Chem. 96 (2022) 107618 https://doi.org/, doi:10.1016/j.compbiolchem.2021.107618.

[6] N.A. AL-Quraan, M.L. Al-Smadi, A.F. Swaleh, GABA metabolism and ROS induction in lentil (Lens culinaris Medik) plants by synthetic 1,2,3-Thiadiazole compounds, J. Plant Interact. 10 (2015) 185–194, doi:10.1080/17429145.2015.1056262.

[7] V. Jatav, P. Mishra, S. Kashaw, J.P. Stables, CNS depressant and anticonvulsant activities of some novel 3-[5-substituted 1,3,4-thiadiazole-2-yl]-2-styryl quinazoline-4(3H)-ones, Eur. J. Med. Chem. 43 (2008) 1945–1954 https://doi.org/, doi:10.1016/j.ejmech.2007.12.003.

[8] A. Bahadur, S. Iqbal, S. Muneer, H.O. Alsaab, N.S. Awwad, H.A. Ibrahium, Synthesis, carbonic anhydrase enzyme inhibition evaluations, and anticancer studies of sulfonamide based thiadiazole derivatives, Bioorg. Med. Chem. Lett. 57 (2022) 128520 https://doi.org/, doi:10.1016/j.bmcl.2021.128520.

[9] M. Madhu Sekhar, U. Nagarjuna, V. Padmavathi, A. Padmaja, N.V. Reddy, T. Vijaya, Synthesis and antimicrobial activity of pyrimidinyl 1,3,4-oxadiazoles, 1,3,4-thiadiazoles and 1,2,4-triazoles, Eur. J. Med. Chem. 145 (2018) 1–10 https://doi.org/, doi:10.1016/j.ejmech.2017.12.067.

[10] E. Matthews, S. Portaro, Q. Ke, R. Sud, A. Haworth, M.B. Davis, R.C. Griggs, M.G. Hanna, Acetazolamide efficacy in hypokalemic periodic paralysis and the predictive role of genotype, Neurology 77 (2011) 1964 1960 LP–, doi:10.1212/WNL.0b013e31823a0cb6.

[11] J. Jiang, X. Li, M. Hanif, J. Zhou, D. Hu, S. Su, Z. Xie, Y. Gao, B. Yang, Y. Ma, Pyridal[2,1,3]thiadiazole as strong electron-withdrawing and less sterically-hindered acceptor for highly efficient donor–acceptor type NIR materials, J. Mater. Chem. C. 5 (2017) 11053–11058, doi:10.1039/C7TC03978F.

[12] T. Ghosh, M. Lehmann, Recent advances in heterocycle-based metal-free calamitics, J. Mater. Chem. C. 5 (2017) 12308–12337, doi:10.1039/C7TC03502K.

[13] D. Bora, A. Kaushal, N. Shankaraiah, Anticancer potential of spirocompounds in medicinal chemistry: A pentennial expedition, Eur. J. Med. Chem. 215 (2021) 113263 https://doi.org/, doi:10.1016/j.ejmech.2021.113263.

[14] L.M.T. Frija, A.J.L. Pombeiro, M.N. Kopylovich, Building 1,2,4-Thiadiazole: Ten Years of Progress, European J. Org. Chem. 2017 (2017) 2670–2682 https://doi.org/, doi:10.1002/ejoc.201601642.

[15] R. Ramachandran, M. Rani, S. Senthan, Y.T. Jeong, S. Kabilan, Synthesis, spectral, crystal structure and in vitro antimicrobial evaluation of imidazole/benzotriazole substituted piperidin-4-one derivatives, Eur. J. Med. Chem. 46 (2011) 1926–1934 https://doi.org/, doi:10.1016/j.ejmech.2011.02.036.

[16] A. Sethukumar, P.S. Anand, C.U. Kumar, B.A. Prakasam, Synthesis, stereochemical and biological studies of some N-cyclohexylcarbamoyl -2,6-diarylpiperidin-4-ones, J. Mol. Struct. 1130 (2017) 352–362 https://doi.org/, doi:10.1016/j.molstruc.2016.10.035.

[17] G. Aridoss, S. Balasubramanian, P. Parthiban, S. Kabilan, Synthesis and NMR spectral studies of N-chloroacetyl-2,6-diarylpiperidin-4-ones, Spectrochim. Acta Part A Mol. Biomol. Spectrosc. 68 (2007) 1153–1163 https://doi.org/, doi:10.1016/j.saa.2007.01.013.

[18] S. Ponnuswamy, S. Sethuvasan, K. Thirunavukarasu, Synthesis, characterisation, stereochemistry and dynamic NMR studies of N-nitroso and N-formyl-t-3-isopropyl-r-2,c-6-bis(4-methoxyphenyl)piperidin-4-ones, J. Mol. Struct. 1089 (2015) 86–94 https://doi.org/, doi:10.1016/j.molstruc.2015.02.045.

[19] J. Chakkaravarthy, G. Muthukumaran, K. Pandiarajan, Conformational study of some N-acyl-2r,6c-diphenylpiperidin-4-one oximes using NMR spectra, J. Mol. Struct. 889 (2008) 297–307 https://doi.org/, doi:10.1016/j.molstruc.2008.02.008.

[20] B. Gates, Responding to Covid-19 — A Once-in-a-Century Pandemic? N. Engl. J. Med. 382 (2020) 1677–1679, doi:10.1056/NEJMp2003762.

[21] M.J. Ali, M. Hanif, M.A. Haider, M.U. Ahmed, F.N.U. Sundas, A. Hirani, I.A. Khan, K. Anis, A.H. Karim, Treatment Options for COVID-19: A Review, Front. Med. 7 (2020) 480 https://www.frontiersin.org/article/10.3389/fmed.2020.00480.

[22] R. Batra, H. Chan, G. Kamath, R. Ramprasad, M.J. Cherukara, S.K.R.S. Sankaranarayanan, Screening of Therapeutic Agents for COVID-19 Using Machine Learning and Ensemble Docking Studies, J. Phys. Chem. Lett. 11 (2020) 7058–7065, doi:10.1021/acs.jpclett.0c02278.

[23] I. Khater, A. Nassar, In silico molecular docking analysis for repurposing approved antiviral drugs against SARS-CoV-2 main protease, Biochem. Biophys. Reports. 27 (2021) 101032 https://doi.org/, doi:10.1016/j.bbrep.2021.101032.

[24] S. Kumar, P.P. Sharma, U. Shankar, D. Kumar, S.K. Joshi, L. Pena, R. Durvasula, A. Kumar, P. Kempaiah, B.Rathi Poonam, Discovery of New Hydroxyethylamine Analogs against 3CLpro Protein Target of SARS-CoV-2: Molecular Docking, Molecular Dynamics Simulation, and Structure–Activity Relationship Studies, J. Chem. Inf. Model. 60 (2020) 5754–5770, doi:10.1021/acs.jcim.0c00326.

[25] M. Rani, S. Jayanthi, S. Kabilan, R. Ramachandran, Spectral Synthesis, Crystal structure, Hirshfeld surface, Computational analysis, and Antimicrobial studies of Ethyl-(E)-4-(2-(2-arylidenehydrazinyl)-2-oxoethyl)piperazine-1-carboxylates, J. Mol. Struct. 1252 (2022) 132082 https://doi.org/, doi:10.1016/j.molstruc.2021.132082.

[26] R. Rajamanickam, S. Sivakolunthu, J. Sampathkumar, Synthesis, crystal structure, Hirshfeld surface, DFT and docking studies of 4-[(5–hydroxy-3-methyl-1-phenyl-1H-pyrazol-4-yl)(phenyl)methyl]-5-methyl-2-phenyl-1,2-dihydro-3H-pyrazol-3-one, J. Mol. Struct. 1252 (2022) 132170 https://doi.org/, doi:10.1016/j.molstruc.2021.132170.

[27] R. Ramachandran, M. Rani, S. Kabilan, Synthesis, structure and conformational analysis of 2,4-diaryl-3-azabicyclo[3.3.1]nonan-9-one thiosemicarbazones and semicarbazones, J. Mol. Struct. 970 (2010) 42–50 https://doi.org/, doi:10.1016/j.molstruc.2010.02.005.

[28] M. Rani, R. Ramachandran, S. Kabilan, Efficient synthesis, spectral analysis and antimicrobial studies of nitrogen and sulfur containing spiro heterocycles from 2,4-diaryl-3-azabicyclo[3.3.1]nonan-9-ones, Bioorg. Med. Chem. Lett. 20 (2010) 6637–6643 https://doi.org/, doi:10.1016/j.bmcl.2010.09.021.

[29] G.M. Sheldrick, SHELXL-97 No Title, Univ. Gottingen, Gottingen, Ger, 1997.

[30] L.J. Farrugia, Ortep-3 for Windows, J. Appl. Cryst. 30 (1997) 565.

[31] P.R. Spackman, M.J. Turner, J.J. McKinnon, S.K. Wolff, D.J. Grimwood, D. Jayatilaka, M.A. Spackman, CrystalExplorer: a program for Hirshfeld surface analysis, visualization and quantitative analysis of molecular crystals, J. Appl. Crystallogr. 54 (2021) 1006–1011, doi:10.1107/s1600576721002910.

[32] D. Shobana, S. Sudha, D. Ramarajan, D. Dimić, Synthesis, crystal structure, spectral characterization and Hirshfeld surface analysis of (E)-N′-(3-ethoxy-4-hydroxybenzylidene)-4-fluorobenzohydrazide single-crystal – a novel NLO active material, J. Mol. Struct. 1250 (2022) 131856 https://doi.org/, doi:10.1016/j.molstruc.2021.131856.

[33] G.W.T.M.J. Frisch, H.B. Schlegel, G.E. Scuseria, M.A. Robb, J.R. Cheeseman, G. Scalmani, V. Barone, G.A. Petersson, H. Nakatsuji, X. Li, M. Caricato, A. Marenich, J. Bloino, B.G. Janesko, R. Gomperts, B. Mennucci, H.P. Hratchian, J.V. Ortiz, A.F. Izma, Gaussian 09,Revision A.02 No Title, Gaussian, Inc, Wallingford, CT, USA, 2013.

[34] AIMAll (Version 19.10.12), Todd A. Keith, TK Gristmill Software, Overland Park KS, USA, 2019

[35] T. Lu, F. Chen, Multiwfn: a multifunctional wavefunction analyzer, J Comput Chem 33 (2012) 580–592, doi:10.1002/jcc.22885.

[36] S. Forli, R. Huey, M.E. Pique, M.F. Sanner, D.S. Goodsell, A.J. Olson, Computational protein–ligand docking and virtual drug screening with the AutoDock suite, Nat. Protoc. 11 (2016) 905–919, doi:10.1038/nprot.2016.051.

[37] BIOVIA, Discovery studio visualizer 4.5, Dassault Systèmes (2016).

[38] R.M. Silverstein Webster, X. Francis, David J. Kiemle, David L. Bryce, Spectrometric identification of organic compounds, 8th ed. (2015).

[39] L. Lunazzi, D. Macciantelli, D. Tassi, A. Dondoni, Conformational studies by dynamic nuclear magnetic resonance. Part 17. Stereodynamic processes in hindered piperidyl-amides and -amidines, J. Chem. Soc. Perkin Trans. 2 (1980) 717–723, doi:10.1039/P29800000717.

[40] P. Parthiban, G. Aridoss, P. Rathika, V. Ramkumar, S. Kabilan, Synthesis, stereochemistry and antimicrobial studies of novel oxime ethers of aza/diazabicycles, Bioorg. Med. Chem. Lett. 19 (2009) 6981–6985 https://doi.org/, doi:10.1016/j.bmcl.2009.10.042.

[41] D. Cremer, J.A. Pople, General definition of ring puckering coordinates, J. Am. Chem. Soc. 97 (1975) 1354–1358, doi:10.1021/ja00839a011.

[42] A. Akila, S. Ponnuswamy, V. Shreevidhyaa Suressh, G. Usha, Synthesis, characterization and stereochemistry of N-acyl-r-2,c-4-bis(4-methoxyphenyl)-3-azabicyclo[3.3.1]nonanes, J. Mol. Struct. 1093 (2015) 113–118 https://doi.org/, doi:10.1016/j.molstruc.2015.03.052.

[43] O. Carugo, G. Resnati, P. Metrangolo, Chalcogen Bonds Involving Selenium in Protein Structures, ACS Chem. Biol. 16 (2021) 1622–1627, doi:10.1021/acschembio.1c00441.

[44] R. Zeng, Z. Gong, Q. Yan, Chalcogen-Bonding Supramolecular Polymers, J. Org. Chem. 85 (2020) 8397–8404, doi:10.1021/acs.joc.0c00723.

[45] S.P. Thomas, D. Jayatilaka, T.N. Guru Row, S···O chalcogen bonding in sulfa drugs: insights from multipole charge density and X-ray wavefunction of acetazolamide, Phys. Chem. Chem. Phys. 17 (2015) 25411–25420, doi:10.1039/C5CP04412J.

[46] S. Umamatheswari, S. Kabilan, Spectral characterization and crystal structure of 5-spiro-(3-methyl-2,6-diphenyltetrahydropyran-4-yl)-4,5-dihydro-[1,3,4]thiadiazole, J. Mol. Struct. 938 (2009) 142–149 https://doi.org/, doi:10.1016/j.molstruc.2009.09.016.

[47] M.A.A. Ibrahim, E.M.Z. Telb, σ-Hole and Lone-Pair Hole Interactions in Chalcogen-Containing Complexes: A Comparative Study, ACS Omega 5 (2020) 21631–21640, doi:10.1021/acsomega.0c02362.
[48] S. Jindani, B. Ganguly, Exploiting the role of stereoelectronic effects to design the antagonists of the human complement C3a receptor, New J. Chem. 45 (2021) 9443–9455, doi:10.1039/D1NJ00730K.
[49] E. Kavitha, D. Ramarajan, A. Rakić, D. Dimić, S. Sudha, P.N. Nirmala, Structural, spectroscopic, quantum chemical, and molecular docking investigation of (E)-N'-(2,5-dimethoxybenzylidene)picolinohydrazide, J. Mol. Struct. 1253 (2022) 132259 https://doi.org/, doi:10.1016/j.molstruc.2021.132259.
[50] S.V Meille, A. Farina, F. Bezziccheri, M.C. Gallazzi, The influence of alkoxy side chains on the conformational flexibility of oligo- and polythiophenes, Adv. Mater. 6 (1994) 848–851 https://doi.org/, doi:10.1002/adma.19940061109.
[51] R. Al-Salahi, H.A. Abuelizz, H.A. Ghabbour, R. El-Dib, M. Marzouk, Molecular docking study and antiviral evaluation of 2-thioxo-benzo[g]quinazolin-4(3H)-one derivatives, Chem. Cent. J. 10 (2016) 21, doi:10.1186/s13065-016-0168-x.
[52] Z. Jin, X. Du, Y. Xu, Y. Deng, M. Liu, Y. Zhao, B. Zhang, X. Li, L. Zhang, C. Peng, Y. Duan, J. Yu, L. Wang, K. Yang, F. Liu, R. Jiang, X. Yang, T. You, X. Liu, X. Yang, F. Bai, H. Liu, X. Liu, L.W. Guddat, W. Xu, G. Xiao, C. Qin, Z. Shi, H. Jiang, Z. Rao, H. Yang, Structure of Mpro from SARS-CoV-2 and discovery of its inhibitors, Nature 582 (2020) 289–293, doi:10.1038/s41586-020-2223-y.
[53] X. Xiaoyu, Y. Hongwei, Y. Haitao, X. Fei, W. Zhixin, S. Wei, L. Jun, Z. Zhe, D. Yi, Z. Qi, Z.X. C, L. Ming, B. Mark, R. Zihe, Structures of Two Coronavirus Main Proteases: Implications for Substrate Binding and Antiviral Drug Design, J. Virol. 82 (2008) 2515–2527, doi:10.1128/JVI.02114-07.
[54] H. Yang, W. Xie, X. Xue, K. Yang, J. Ma, W. Liang, Q. Zhao, Z. Zhou, D. Pei, J. Ziebuhr, R. Hilgenfeld, K.Y. Yuen, L. Wong, G. Gao, S. Chen, Z. Chen, D. Ma, M. Bartlam, Z. Rao, Design of Wide-Spectrum Inhibitors Targeting Coronavirus Main Proteases, PLOS Biol 3 (2005) e324, doi:10.1371/journal.pbio.0030324.
[55] Y. Shimamoto, Y. Hattori, K. Kobayashi, K. Teruya, A. Sanjoh, A. Nakagawa, E. Yamashita, K. Akaji, Fused-ring structure of decahydroisoquinolin as a novel scaffold for SARS 3CL protease inhibitors, Bioorg. Med. Chem. 23 (2015) 876–890 https://doi.org/, doi:10.1016/j.bmc.2014.12.028.
[56] M. Wang, R. Cao, L. Zhang, X. Yang, J. Liu, M. Xu, Z. Shi, Z. Hu, W. Zhong, G. Xiao, Remdesivir and chloroquine effectively inhibit the recently emerged novel coronavirus (2019-nCoV) in vitro, Cell Res 30 (2020) 269–271, doi:10.1038/s41422-020-0282-0.
[57] B. Nutho, P. Mahalapbutr, K. Hengphasatporn, N.C. Pattaranggoon, N. Simanon, Y. Shigeta, S. Hannongbua, T. Rungrotmongkol, Why Are Lopinavir and Ritonavir Effective against the Newly Emerged Coronavirus 2019? Atomistic Insights into the Inhibitory Mechanisms, Biochemistry 59 (2020) 1769–1779, doi:10.1021/acs.biochem.0c00160.
[58] M.M. Ghahremanpour, J. Tirado-Rives, M. Deshmukh, J.A. Ippolito, C.-H. Zhang, I. Cabeza de Vaca, M.-E. Liosi, K.S. Anderson, W.L. Jorgensen, Identification of 14 Known Drugs as Inhibitors of the Main Protease of SARS-CoV-2, ACS Med. Chem. Lett. 11 (2020) 2526–2533, doi:10.1021/acsmedchemlett.0c00521.
[59] R. Hatada, K. Okuwaki, Y. Mochizuki, Y. Handa, K. Fukuzawa, Y. Komeiji, Y. Okiyama, S. Tanaka, Fragment Molecular Orbital Based Interaction Analyses on COVID-19 Main Protease – Inhibitor N3 Complex (PDB ID: 6LU7), J. Chem. Inf. Model. 60 (2020) 3593–3602, doi:10.1021/acs.jcim.0c00283.
[60] Ž.B. Milanović, M.R. Antonijević, A.D. Amić, E.H. Avdović, D.S. Dimić, D.A. Milenković, Z.S. Marković, Inhibitory activity of quercetin, its metabolite, and standard antiviral drugs towards enzymes essential for SARS-CoV-2: the role of acid–base equilibria, RSC Adv 11 (2021) 2838–2847, doi:10.1039/D0RA09632F.